

# **Magma-carbonate interaction processes and associated CO<sub>2</sub> release at Merapi volcano, Indonesia: insights from experimental petrology**

F.M. Deegan<sup>1</sup>, V.R. Troll<sup>1,2</sup>, C. Freda<sup>2</sup>, V. Misiti<sup>2</sup>, J.P. Chadwick<sup>3</sup>, C. McLeod<sup>4</sup>, & J.P. Davidson<sup>4</sup>.

<sup>1</sup>Department of Earth Sciences, Uppsala University, Villavägen 16, Uppsala, Sweden

<sup>2</sup>Istituto Nazionale di Geofisica e Vulcanologia, Rome, Italy

<sup>3</sup>Department of Petrology (FALW), Vrije Universiteit, Amsterdam, Netherlands

<sup>4</sup>Durham University, Durham, United Kingdom

Corresponding authors: Frances Deegan [Email: Frances.Deegan@geo.uu.se]; Valentin R Troll [Email: Valentin.Troll@geo.uu.se], Carmela Freda [Email: freda@ingv.it].

## ABSTRACT

There is considerable evidence for ongoing, late-stage interaction between the magmatic system at Merapi volcano, Indonesia, and local crustal carbonate. Calc-silicate xenoliths within Merapi basaltic-andesite erupted rocks display textures indicative of intense interaction between magma and crustal carbonate, and Merapi feldspar phenocrysts frequently contain individual crustally contaminated cores and zones. In order to resolve the interaction processes between magma and limestone in detail, we have performed a series of time-variable de-carbonation experiments in silicate melt, at magmatic pressure and temperature, using Merapi basaltic-andesite and local Javanese limestone as starting materials. We have used in-situ analytical methods to determine the elemental and strontium isotope composition of the experimental products and to trace the textural, the chemical, and the isotopic evolution of carbonate assimilation. The major processes of magma-carbonate interaction identified are: i) rapid decomposition and degassing of carbonate, ii) generation of a Ca-enriched, highly radiogenic strontium contaminant melt, distinct from the starting material composition, iii) intense CO<sub>2</sub> vesiculation, particularly within the contaminated zones, iv) physical mingling between the contaminated and unaffected melt domains, and v) chemical mixing between melts. The experiments reproduce many of the features of magma-carbonate interaction observed in the natural Merapi xenoliths and feldspars phenocrysts. The Ca-rich, high <sup>87</sup>Sr/<sup>86</sup>Sr contaminant melt produced in experiment is here considered as a pre-cursor to the Ca-rich (often “hyper-calcic”) phases found in the xenoliths and the contaminated zones in Merapi feldspar. The xenoliths also exhibit micro-vesicular textures which can be linked to the CO<sub>2</sub> liberation process seen in experiment. This study, therefore, provides well-constrained petrological insights into the problem of crustal interaction at Merapi and points toward the substantial impact of such interaction on the volatile budget of the volcano.

Key words: *carbon dioxide; experimental petrology; magma-carbonate interaction; strontium isotopes*

## INTRODUCTION

Volcanoes sited on subduction zones are the most dangerous on the planet. Merapi volcano in Central Java, Indonesia, is one such hazardous volcano with both historical and recent explosive eruptions (Voight *et al.* 2000 and references therein; Donoghue *et al.*, 2009). Merapi is one of the most active volcanoes on Java and is located less than 30km north of Yogyakarta – the largest city in Central Java with a population of ca. 3.5 million (**Fig 1 a, b**).

The role of intra-crustal contamination in volcanic arc settings is a source of on-going debate (e.g. Davidson *et al.*, 2005). Its occurrence, however, has been well documented at many volcanic centres located in arc settings such as the Lesser Antilles arc (e.g. Smith *et al.*, 1996; Macdonald *et al.*, 2000 and references therein), the Kermadec arc (e.g. Macpherson *et al.*, 1998; Smith *et al.*, 2006), and the Sunda arc in Indonesia (e.g. Gasparon *et al.*, 1994, Gasparon & Varne, 1998). Merapi is an arc volcano beneath which the upper crust consists of Cretaceous to Tertiary limestone, marl, and volcanoclastic units up to 2km thick (van Bemmelen, 1949). Sedimentary units in the Central Java area extend further down and the currently active central Javan volcanic arc is partly sited on the Kendang sedimentary basin, whose sediment thickness ranges from 8 to 11km (Smyth *et al.*, 2005 and references therein). This is underlain, in turn, by a basement of uncertain character extending to a depth of ca. 25km (Curry *et al.*, 1977; Hamilton, 1979). Recent erupted products at Merapi display strong evidence for magma-crust interaction (Chadwick *et al.*, 2007), including abundant calc–silicate xenoliths, which frequently exhibit well–developed, skarn-type, vesicular reaction rims. Crystal isotope stratigraphy and major element profiling of plagioclase phenocrysts in recent Merapi basaltic–andesite has identified carbonate assimilation and xenolith recycling as a process affecting magma composition and potentially the volatile budget at Merapi (Chadwick *et al.*, 2007). Merapi feldspars presented by these authors are variably zoned: i) plagioclases with albitic cores mantled by anorthitic rims (An<sub>80-90</sub>), with radiogenic <sup>87</sup>Sr/<sup>86</sup>Sr ratios in the rims, indicate the presence of a Ca–rich, crustally–derived liquid during crystallisation; and

ii) plagioclases with anorthitic cores (with up to almost An<sub>100</sub>) and crustal <sup>87</sup>Sr/<sup>86</sup>Sr ratios in the cores but less calcic and less radiogenic rim compositions. These latter types are interpreted as inherited, calc–silicate derived crystal cores. Note that magma–carbonate interaction of similar character has also been identified at other volcanic systems emplaced within carbonate-rich crust, such as the Alban Hills, Italy (Freda *et al.*, 1997; Dallai, *et al.*, 2004); Vesuvius, Italy (Gilg *et al.*, 2001; Del Moro *et al.*, 2001; Fulignati *et al.*, 2004), and Popocatepétl volcano, Mexico (Goff *et al.*, 2001; Schaaf *et al.*, 2005), all of which, like Merapi, are prone to explosive eruptive behaviour.

While considerable textural and geochemical ‘end–product’ evidence for interaction between Merapi magma and crustal carbonate exists, detailed understanding of the mechanisms and rates of magma–carbonate interplay producing such textures and the associated chemical exchanges at the magma–crust interface is very limited. To address this problem, we have designed a time–constrained experimental series investigating the de–carbonation and contamination processes of magma–carbonate interaction in a controlled laboratory environment. Experimental petrology techniques have previously been used to examine the processes of assimilation and contamination in magmatic systems (e.g. Watson, 1982; Watson & Jurewicz, 1984; Johnston & Wyllie, 1988; Beard *et al.*, 1993; Sachs & Strange, 1993; McLeod & Sparks, 1998; Knesel & Davidson, 2002; García-Moreno *et al.*, 2006), however, our experimental design differs significantly from previous works on two key points. Firstly, we focus on assimilation of crustal carbonate by magma, which is less frequently addressed in the literature than fusion and assimilation of silicic crustal components. Some experimental studies of limestone assimilation by magma have been carried out previously, contrasting the present study in that they have largely focussed on the phase assemblages resulting from carbonate digestion, rather than on the initial processes and progression of carbonate assimilation (see Freda *et al.*, 2008a; Iacono Marziano *et al.*, 2008; Mollo *et al.*, 2010). Secondly, we have carried out experiments using very short and progressively increasing dwell times (0 to 300s), much shorter than those of any other experimental study of xenolith assimilation in the

literature in which experiments typically run for hours to days. These design considerations allow for preservation of transient textures in the experimental products, and for examination of some features of mass transport and intra-melt homogenisation at the contaminated melt front as carbonate assimilation proceeds. We have carried out piston cylinder experiments at  $T = 1200^{\circ}\text{C}$  and  $P = 0.5 \text{ GPa}$ , which corresponds to a relatively deeply seated system (15-20km) compared to where carbonate assimilation is largely expected to occur (in the upper 10km of the crustal section beneath Merapi, **Fig 1 c**). We applied a pressure of 0.5 GPa as this is the lowest pressure that the piston cylinder apparatus is calibrated for. Our system hence closely simulates the deepest conditions under which carbonate assimilation will initiate and our results can, in turn, be sensibly extrapolated to a shallower system. With respect to the rate of decarbonation, it will proceed considerably faster under lower pressures. This means that the timescales of carbonate assimilation estimated from our experiments represent a maximum of what we can expect in nature under similar conditions to our experimental system.

Also note that the limestone grain is heated concurrently with the starting M-94 powdered glass, which may initially appear to represent a thermal limitation to the methodology. Considering some aspects of the magmatic system at Merapi, however, such as its long-lived nature (the onset of volcanism is estimated at 40,000 years BP, Camus *et al.*, 2000) and its high heat flux (Chadwick, 2007; Koulakov *et al.*, 2007; Wagner *et al.*, 2007), the crust underlying Merapi must be already heated to several hundred degrees celsius. We argue that simultaneous heating of the starting materials in our experiments therefore best simulates a long-lived system, such as Merapi (Annen & Sparks, 2002).

By considering the experimental data in combination with the natural products of magma-carbonate interaction (xenoliths and feldspars), we can improve our understanding of deep and shallow contamination processes. The experiments provide insights into the late-stage, short time

scale de-carbonation processes that can seriously affect the eruptive behaviour of volcanoes sitting on carbonate crust with potentially very little forewarning.

## **GEOLOGICAL BACKGROUND**

Merapi volcano is located on the active Sunda arc, in Central Java, Indonesia (**Fig 1 a**). Northward subduction of the Indian Ocean plate beneath the Eurasian plate has been occurring along the Java trench since the middle Eocene (Hamilton, 1979; Hall, 2002). This has resulted in an ancient Eocene to Miocene volcanic zone in the southern part of Java known as the Southern Mountains Zone, and the present day volcanic arc that is distributed along the entire length of the central part of the island, known as the Central Volcanic Zone (Smyth *et al.*, 2007). Van Bemmelen (1949) described several stratigraphic–tectonic zones along Java, of which the major zones, from South to North, are: the Southern Mountains Zone, the Central Volcanic Zone, the Kendeng Zone, and the Rembang Zone. The presently active Central Volcanic Zone is partly sited on the Kendeng Zone, which is the main Eocene–Miocene sedimentary basin in East Java, comprising 8–11km thick successions of volcanoclastic and marine sediments, including abundant limestone units up to 2km thick (van Bemmelen, 1949; de Genevraye & Samuel, 1972; Untung & Sato, 1978; Smyth *et al.*, 2005). Merapi is the youngest of a cross-arc NNW-trending chain of volcanoes, including Telemoyo, Merbabu, and Merapi, which are bound by the Southern Mountains and the Kendeng Zones (**Fig 1 b**). The nature of the basement beneath Merapi is intermediate between oceanic and continental crust (Curry *et al.*, 1977), with Merapi sited close to a structural lineation referred to as the Progo–Muria fault, thought to delimit the extent of Cretaceous continental basement beneath Java (Smyth *et al.*, 2005, **Fig 1 a**). Geobarometric and tomographic methods applied to Merapi volcano and basement as presented by Chadwick (2008) indicates that an interconnected network of melt bodies is likely to exist beneath the edifice in a diffuse zone from a depth of ca. 3km to ca. 31km beneath the summit (summit elevation is ca. 3,000m) (**Fig 1 c**). Such a plumbing system

beneath the volcano provides ample opportunity for interaction between magma and upper to mid crustal lithologies, including abundant carbonate rocks in the top 10km.

Of the 89 Indonesian volcanoes with historical eruptions (van Bemmelen, 1949), Merapi is one of the most active and destructive. Recent volcanism at Merapi is characterised by the growth of viscous lava domes followed by collapse of the dome complex and resultant pyroclastic block and ash flows (BAFs or nuées ardentes, e.g. Abdurachman *et al.*, 2000; Schwarzkopf *et al.*, 2001, 2005; Charbonnier & Gertisser, 2008; Donoghue *et al.*, 2009). The volcanic products are basaltic-andesite in composition and contain abundant inclusions, of which thermally metamorphosed calc-silicate types are common (e.g. Clochiatti *et al.*, 1982; Camus *et al.*, 2000 and references therein). The various types of inclusions hosted within Merapi lavas are described in Troll *et al.* (2003) and a detailed petrographic and geochemical description of a selection of typical Merapi calc-silicate xenoliths, including those presented here, is given in Chadwick *et al.* (2007). Hand specimen examples of the xenoliths described in this paper, with noteworthy macroscopic features such as vesicular textures and neo-mineralised skarn contact zones between magma and xenoliths, are shown in **Fig 2**. The presence of such metamorphosed limestone xenoliths are the primary motivation for our experimental study as they indicate on-going, albeit poorly constrained, magma-carbonate interaction beneath Merapi, that we hypothesise to have significant repercussions for the volcano's short-term volatile budget and consequent eruptive behaviour.

## **EXPERIMENTAL METHOD**

All of the experiments in this study were carried out using the piston cylinder apparatus at the HP-HT Laboratory of Experimental Volcanology and Geophysics at the Istituto Nazionale di Geofisica e Vulcanologia (INGV) Rome. The piston cylinder is calibrated to perform experiments in the pressure range 0.5–2 GPa. All experiments reported here were carried out at the lowest end of this range, at 0.5 GPa, which corresponds to a mid-crustal depth of approximately 15km (note that total crustal thickness in Java is ca. 25km) (Curry *et al.*, 1977; Hamilton, 1979). Pressure equivalent to

shallower crustal depths could not be applied using the piston cylinder. However, the piston cylinder has a major advantage over low-pressure experimental devices, which is its rapid heating and quench rate. The piston cylinder apparatus reaches 1200 °C after only 6 minutes, which is sufficiently fast to allow preservation of the carbonate phase in the shortest duration experiments and subsequent inspection of the interaction between carbonate and melt over a time-scale of minutes after the experimental temperature is reached. It is for this reason that the piston cylinder was selected as the most appropriate instrument for this study. Given that the magmatic system beneath Merapi extends from ca. 3km to 31km depth (Chadwick, 2008), the mid to upper parts of the system must be emplaced into the sedimentary sequences that attain thicknesses of maximum 11km (Smyth *et al.*, 2005 and references therein). Our experimental approach, therefore, is a close replication of the physical conditions at which initial magma-carbonate interaction is likely to occur, i.e. the deep to mid level parts of the magma system at Merapi.

### **Starting materials**

The experimental series can be divided into two sub-series that were run in tandem: experiments using a nominally anhydrous starting material and experiments using a hydrated starting material. Each experimental run contained one anhydrous and one hydrated experiment to allow a direct comparison at each given set of parameters. The starting material for all experiments was a sample of Merapi basaltic-andesite (sample M-94-a-107, courtesy L.M. Schwarzkopf) from the 1994 block and ash flow deposits. Sample M-94-a-107 was chosen for use in experiment as it is representative of the most recent volcanic material produced at Merapi, and is host to many calc-silicate xenoliths. M-94-a-107 is a grey ( $M \approx 50-60$ ) finely crystalline rock with up to 45% phenocrysts by volume, predominately plagioclase, with some clinopyroxene crystals and minor amounts of amphibole. The sample was crushed into 1–2 mm sized chips, hand-picked for pristine appearance, and then ground to powder in a WC Tema mill. The powdered sample was subsequently fused, in order to produce a glass of primitive and homogeneous basaltic-andesite composition. The nominally anhydrous glass



was produced at the Università degli Studi Roma Tre, Italy by melting an aliquot of the M-94-a-107 powder at 1300°C and 1 atm in a rapid-quench furnace. The hydrous glass, in turn, was produced at the Universität Hannover, Germany by doping the M-94 powder with ca. 2 wt% H<sub>2</sub>O and melting in an internally heated pressure vessel at 1200°C at 0.2 GPa. The hydrated glass was analysed for its water content by Karl Fischer Titration (KFT) at Hannover, Germany (for details of the KFT method see Behrens, 1995). Both sets of glass (anhydrous and hydrous) were analysed for their composition (**Table 1**) and verified to be free of crystals and crystallites by BSE imaging using the electron microprobe at INGV Rome. The glasses were then hand-ground to powder using an agate mortar and pestle before insertion into the experiment capsules.

The calcium carbonate added to the experimental charges are samples of local crust sourced from a carbonate platform south of Merapi, at the town of Parangtritis (see Chadwick *et al.*, 2007 for sample location and **Fig 1 b**). The limestone sample was cut into solid cubes of ca. 3mm side length (ca. 9–10 mg) for use in the experiments. The composition of the carbonate starting material (**Table 1**) was determined by XRF (for major elements) and infra-red photometry (for CO<sub>2</sub> content) at IFM-GEOMAR, Kiel, Germany following the methodology given in Abratis *et al.* (2002).

### **Experimental conditions and procedure**

All of the experiments presented in this paper were carried out at 1200°C and 0.5 GPa (**Table 2**), except for one experimental run at 1 GPa to test for additional pressure effects. The dwell time ( $t_d$ ) is the length of time that the experiment was held at the experimental temperature. This parameter was varied from  $t_d = 0$ s (i.e. immediate quenching upon reaching 1200°C) to  $t_d = 300$ s. Experiments were carried out at super-liquidus temperature for hydrated Merapi basaltic-andesite. This temperature has been used in Merapi assimilation and fractional crystallisation models (AFC) by Chadwick *et al.* (2007) and is verified as super-liquidus temperature here for the hydrated starting composition by running melting experiments, without carbonate, at 1200°C with  $P = 0.5$  GPa and  $t_d = 300$ s. These experiments yielded crystal-free products and are consistent with two-pyroxene

thermometry of 1994 Merapi BAF samples presented in Gertisser (2001) that yielded a pyroxene crystallisation temperature (sub-liquidus) of  $1007 \pm 12^\circ\text{C}$ .

Platinum capsules with 3.0mm outer diameter were used for all experiments. Capsules were welded at one end using an arc welder and loaded with the powdered M-94 glass to fill ca. 1/5th of the capsule volume. This was followed by inserting a cube of limestone (8.5 to 10.3 mg), after which the capsule was loaded with more powdered M-94 glass (38 to 42 mg) (see **Table 2**). The ratio of powder inserted before the carbonate and that after, was kept similar for all runs. The capsules were then welded at the open end and positioned into a 19.1mm NaCl-crushable alumina-pyrex assembly, with capsules containing the hydrated starting material additionally encased in pyrophyllite powder to prevent water loss (*cf.* Freda *et al.*, 2001).

Experiments were pressurised at room temperature to 0.5 GPa and then heated in two stages, from ambient temperature to  $1180^\circ\text{C}$  at a rate of  $200^\circ\text{C}/\text{min}$ , followed by gradual heating at  $20^\circ\text{C}/\text{min}$  until the experimental temperature was reached. Temperature was controlled by a factory calibrated  $\text{W}_{95}\text{Re}_5\text{-W}_{74}\text{Re}_{26}$  (type C) thermocouple and held within  $\pm 3^\circ\text{C}$  of the experimental temperature. For this type of assembly, temperature gradient along the capsules is around  $10^\circ\text{C}$  (Hudon *et al.*, 1994; Médard *et al.*, 2008). Oxygen fugacity of about  $\text{NNO}+2$  was attained in experiment due to the type of assembly used to encase the charges (Freda *et al.*, 2008a and references therein).

Generally, two capsules were inserted into the experiment assembly (one hydrous and one anhydrous), however, for some runs the assembly was constructed to hold three capsules equidistant from the thermocouple 'hot spot'. This configuration was used to allow, for example, a carbonate-free control experiment to be run under the same conditions as the hydrous and anhydrous decarbonation experiments. Selected runs were repeated in order to verify the reproducibility of the results.

Experiments were terminated by shutting down the power source. In this way the experimental charges were quenched at a rate of ca. 2000°C/min (to the glass transition) and the textural interplay between limestone and the melt was preserved. The experimental capsules were then retrieved, mounted in epoxy resin, opened on one side parallel to their long axes, and polished for microprobe analysis.

## **ANALYTICAL METHODS**

### **Electron microprobe analysis (EMPA)**

Micro-analyses and scanning electron microscopy (SEM) imaging of the experimental products were carried out at INGV Rome, Italy, using a JEOL-JXA8200 EDS-WDS combined instrument, equipped with five wavelength–dispersive spectrometers and twelve crystals. Microprobe WDS analyses were performed using an accelerating voltage of 15 kV, a beam current 5 nA, and a beam diameter of 5µm for glass and 1µm for mineral analyses (see e.g. Iezzi *et al.*, 2008 for analytical details). Sodium and potassium were analysed first to reduce loss on volatisation. Analyses and imaging were carried out over several analytical sessions, with standards optimised for each session. Micro-analyses and SEM imaging of a representative selection of natural Merapi calc–silicate xenoliths were also carried out at INGV Rome using the same analytical conditions as for the experimental products. The average standard deviation ( $1\sigma$ ) of each element in the analysed standards over 5 analytical sessions (including both experiment and xenolith analyses) is as follows: SiO<sub>2</sub> (0.28), TiO<sub>2</sub> (1.86), Al<sub>2</sub>O<sub>3</sub> (0.27), FeO (0.47), MnO (0.33), MgO (0.44), CaO (0.33), Na<sub>2</sub>O (0.41), K<sub>2</sub>O (0.26), P<sub>2</sub>O<sub>5</sub> (0.35).

### **Micro-sampling and analysis of <sup>87</sup>Sr/<sup>86</sup>Sr and trace elements**

Micro-sampling of the experimental products was carried out in the Arthur Holmes Isotope Geology Laboratory at Durham University, UK, using a New Wave™ Micromill™ following the techniques given in Charlier *et al.* (2006) and references therein. The micro-mill apparatus consists of a drill and stage, a binocular microscope, and a computer workstation that integrates all

components, allowing for precise control to ca. 1 $\mu$ m of the location of drill points, the movement of the drill, and the depth of drilling. Suitable sampling areas were selected using back scattered electron (BSE) images of the experiments, taking care to avoid fractures and bubbles. Samples were then mounted as thick sections (up to 500 $\mu$ m thick) prior to micro-milling. The BSE images were used in conjunction with the binocular microscope optics at the drill workstation to locate the optimal sampling areas. Samples were milled in discrete arrays of points to a depth of ca. 90 $\mu$ m per sample by performing two passes of 45 $\mu$ m depth per sample. The size of each sample array varied due to nearby bubbles and fractures which limited the area that could be drilled. Milling was carried out under a drop of ultra-pure Milli-Q water to collect the drilled sample powder. The water and sample powder mixture was then pipetted onto a gold boat and placed in an ultra-clean fume hood to evaporate the water. The sample powder was then dissolved in ultra-pure, distilled acids and the Sr fraction subsequently separated using micro-Sr column chemistry as described by Charlier *et al.* (2006) in preparation for thermal ionisation mass spectrometry (TIMS). Procedural blanks were performed by milling within the water drop, but without touching the sample. The blank was thereafter treated identically to the samples. Samples were analysed at the University of Durham using a Thermo-Finnigan Triton TIMS operating in static mode. Details of the procedure used to load small Sr samples, TIMS running conditions, and data correction is given in Font *et al.* (2008). The Triton was in positive-mode from January – March 2009, during which 78 analyses of the international Sr standard NBS 987 were carried out on loads ranging from 3ng to 600ng. The overall average NBS 987  $^{87}\text{Sr}/^{86}\text{Sr}$  value is  $0.710246 \pm 0.000016$  ( $2\sigma$ ) ( $n = 78$ ), which agrees extremely well with the accepted NBS 987  $^{87}\text{Sr}/^{86}\text{Sr}$  value reported by Thirlwall *et al.* (1991) of  $0.710248 \pm 0.000023$  ( $2\sigma$ ) ( $n = 427$ ). Aliquots of the dissolved samples were also analysed for their trace element concentrations by inductively coupled plasma mass spectrometry (ICPMS) using a Thermo Electron Element II system at Durham University. Procedural details can be found in Font *et al.* (2008). Total procedural blanks ( $n = 3$ ) were less than 19 pg for all elements analysed; Sr

blanks averaged  $0 \pm 1$  pg ( $2\sigma$ ) ( $n = 3$ ). In total, 9 glass samples were micro-milled and analysed from two experiments: 379-17 ( $t_d = 0s$ ) ( $n = 4$ ) and 386-19 ( $t_d = 300s$ ) ( $n = 5$ ).

## EXPERIMENTAL RESULTS

The textural progression of magma–carbonate interaction, in both anhydrous and hydrous experiments, is shown in the BSE images in **Fig 3**, and a summary of the phases detected in each experiment is given in **Table 2**. Images **3 a)** to **3 e)** show the major features of magma–carbonate interaction from  $t_d = 0s$  (immediate quenching at  $1200^\circ\text{C}$ ) to  $t_d = 300s$  for experiments carried out using the nominally anhydrous starting M-94 glass. Images **3 f)** to **3 j)** show the same sequence for experiments carried out using the hydrated ( $\text{H}_2\text{O} = 2.23$  wt%) starting M-94 glass. The major textural features of carbonate assimilation include the development of copious amounts of gas bubbles and the generation of two compositionally distinct domains of glass which can be identified on the BSE images by their contrasting brightness. Note the faster rate of carbonate assimilation in the hydrated series.

Major element profiles (EMPA) were carried out through the carbonate–glass and the intra-glass interfaces in all experiments, where applicable. Representative element variation profiles are shown in **Fig 4** for hydrous experiments only because the glass in hydrous experiments is generally crystal free (only the shorter runs contain calcite crystallites within the Ca-contaminated regions). This allows for examination of the intra-melt transitions, excluding complications due to crystallisation at the interfaces. Furthermore, the hydrous series of experiments more closely represents the natural, ‘wet’ arc–magma system. It is noteworthy, however, that both the anhydrous and the hydrous experiments display similar features in terms of textures, major element composition, and the shapes of the chemical profiles that traverse the glass interfaces. Representative major element analyses of the experimental glasses are given in **Table 3**. The Sr isotope profiles of two hydrous experiments are shown in **Fig 5** and the data reported in **Table 4**. Trace element concentrations in the drilled samples can be found in the electronic appendix.

## Overview of the experimental products

In the anhydrous series, carbonate is preserved in experiments with  $t_d$  up to 150s (**Fig 3 a - d**), but appears to be largely consumed at  $t_d > 150$ s (**Fig 3 e**). Experiments consist of three phases: solid (crystals with or without carbonate), melt (preserved as glass), and an exsolved volatile phase ( $\text{CO}_2$  preserved as vesicles). Crystals of plagioclase (and minor amounts of spinel) always occupy some of the solid phase in the anhydrous experiments, but not in the hydrous ones.

In the hydrous series the rate of carbonate consumption is higher than in the anhydrous experiments, as evidenced by the comparatively lesser amount of carbonate surviving with increasing dwell times. Hydrous experiments with  $t_d \leq 60$ s are similar to their anhydrous counterparts, with three phases detected: solid (carbonate + dendritic calcite crystallites), melt (preserved as glass), and an exsolved volatile phase (predominately  $\text{CO}_2$  preserved as vesicles). Note that adding  $\text{CO}_2$  to the system causes a significant drop in  $\text{H}_2\text{O}$  solubility, which may allow  $\text{H}_2\text{O}$  to occupy some of the volatile phase (Botcharnikov *et al.*, 2005; and see discussion). Hydrous experiments with  $t_d \geq 90$ s are texturally the most simple of the entire experimental series presented in this paper, with just two phases detected: melt (as glass of varying composition) and an exsolved volatile phase (as bubbles).

The melt in the experimental products comprises two compositionally distinct domains that are defined with respect to their calcium content, as this is the most variable major element along with silica. There exists: i) a Ca-normal (or “Merapi-like”) end-member, with CaO content in the range 7.98 – 9.99 wt.% (cf. anhydrous M-94 with CaO wt.% = 8.89 versus hydrous M-94 with CaO wt.% = 9.19), and ii) a Ca-enriched (“contaminated”) end-member, with CaO content up to ca. 36 wt.%. A diffuse, hybrid composition melt zone exists where the Ca-normal and Ca-rich melts are in contact.

## Interfaces in experiment

Carbonate is always bordered by a zone of Ca-enriched glass, which can be distinguished in the BSE images by its brighter appearance, in strong contrast to the adjacent darker, Ca-normal glass. This Ca-rich border zone extends around the carbonate to varying degrees, and is most extensive in hydrous experiments (**Fig 3 f, g**). The contacts between the border zone and the surrounding Ca-normal glass ( $\pm$  crystals) are usually lobate to irregular in shape (**Fig 3**). Calcite quench crystals are observed within the Ca-rich border zone for the shorter duration experiments only ( $t_d = 0s$  and  $60s$ , e.g. **Fig 3 f**). These crystals have a dendritic to feathery morphology indicating rapid undercooling and local calcium super-saturation of the experimental melts.

The contact between the two distinct glass domains (the “glass interfacial zone”, shaded grey on **Fig 4**) is a chemically diffuse zone of variable extent, composed of a hybrid melt composition falling between the Ca-normal and Ca-rich glass end-members (**Table 3**). This glass interfacial zone is defined principally by the coupled change in wt.% of CaO and SiO<sub>2</sub> and is always characterised by progressive calcium-enrichment and simultaneous silica-depletion towards the Ca-rich glass and/or the carbonate (where present). Aluminium is strongly linked to Si activity in the experimental products with the shape of the Al profiles consistently mimicking the Si profiles (**Fig 4 a-c**). The profile shapes of the alkali elements Na<sub>2</sub>O, K<sub>2</sub>O and MgO differ slightly to those of SiO<sub>2</sub>, CaO, and Al<sub>2</sub>O<sub>3</sub>, probably due to the much higher diffusivities of the alkalis (e.g. Freda & Baker, 1998). The Ca-rich glass is generally characterised by depletion in alkalis, with respect to the M-94 starting composition. With the exception of peculiar behaviour at  $t_d = 0s$ , the behaviour of K<sub>2</sub>O and Na<sub>2</sub>O appears to be closely coupled to that of SiO<sub>2</sub> (**Fig 4 d-f**). The glass interfacial zone is also characterised by a mixed <sup>87</sup>Sr/<sup>86</sup>Sr signature between the melt end-members and lies within the <sup>87</sup>Sr/<sup>86</sup>Sr range of Merapi feldspar Sr isotope values (Chadwick *et al.*, 2007) (**Fig 5 and 6 a**).

The length of the glass interface along the EMPA profiles is measured as the mixing distance between end-members from the point where the glass composition begins to deviate from

Ca-enriched to where it returns to the starting composition. Its length is greatest in the longest dwell time experiments, at ca. 450  $\mu\text{m}$ , versus only ca. 80 $\mu\text{m}$  in the 0s experiments, demonstrating a greater degree of mixing in the longer experiments. A simple binary mixing model for the long dwell time experiment (300s), demonstrates a slight enrichment in CaO as the Ca-normal glass domain is approached, which exceeds that expected for simple chemical mixing between end-members (**Fig 7** and see discussion).

### **Inter-carbonate glass**

In experiments where carbonate is still found, Ca-rich glass frequently forms pools and fracture infill within the carbonate grain. Fractures can be extremely small and thread-like and frequently terminate in a triple-junction-type arrangement and are better developed in hydrous experiments than in the anhydrous ones. An excellent example of an experiment displaying these features is shown in **Fig 8 a, b** where the fractures can be seen to form a zigzag interlocked array within the carbonate, with glass-filled pools sited at the meeting point of some of these fractures. The composition of the glass within the carbonate is the same as that of the Ca-enriched glass domain that surrounds the carbonate, indicating that the inter-carbonate glass is a mixture of infiltrating silicate melt and dissolved carbonate rather than a pure *in-situ* carbonate melt. Representative analyses of the inter-carbonate glass are given in **Table 3**.

### **Vesicle distribution**

Carbon dioxide vesicles are present in all experiments. The quantity, size, and distribution of vesicles vary, however, throughout the series. Multiple vesicle populations are identified in many of the experiments, in particular those in which carbonate is found, surrounded by a characteristic Ca-rich melt border. In these cases, the largest vesicles (up to 700 $\mu\text{m}$  across) are always found within the Ca-rich glass domain (**Fig 3 a, b, c, d**). This zone also frequently hosts a micro-bubble front at its furthest margin from the carbonate and at the carbonate – glass contact (**Fig 8 c**, three generations of vesicles can be observed). In experiments where the carbonate can no longer be



found, the largest bubbles are consistently found within the Ca-enriched glass domain. The maximum vesicle size measured for this experimental series is 1.39 mm in a hydrous experiment of 300s duration (**Fig 3 j** and **9 b**), suggesting that bubbles tend to coalesce with increasing experimental run-time. Overall vesicle distribution patterns are similar in both the anhydrous and hydrous series but vesicle density is greater in the hydrous series (see Misiti *et al.*, 2008). In comparison, vesiculation is much more vigorous in the carbonated experiments than in the corresponding control experiments in which no carbonate was added. In the hydrous control experiment(s) vesicles are randomly distributed and vesicle size is more or less constant at about 1 $\mu$ m whereas relatively large vesicles up to 1.97mm across can be found within the Ca-contaminated glass where limestone has been added to the capsule. The 1 $\mu$ m vesicles observed in the control experiments can also be found in the “unaffected” regions in the de-carbonation experiments and probably represent mere “shrinkage bubbles”.

#### **Testing for pressure effects: 1 GPa experiment**

Although we could not test the effect of lowering the pressure to < 0.5 GPa on the experimental system, we performed a 300s hydrated experiment at 1 GPa to test the influence of increasing the pressure. The result of this experiment is shown in the BSE image in **Fig 9**, alongside a 0.5 GPa equivalent experiment for direct comparison. The 1 GPa experiment is texturally similar to the 0.5 GPa experiment, and the vesicles produced are similarly sized.

#### **NATURAL MERAPI CALC-SILICATE XENOLITHS**

To complement our experimental data, we made detailed observations on two selected and representative calc-silicate xenoliths within Merapi basaltic-andesite. Sample MXCS-0 (cut into seven sections, a – g) and sample MXCS-1 (cut into two sections, a and b) are shown at hand-specimen scale in **Fig 2**. These xenoliths have previously been described in terms of their mineralogy, whole-rock geochemistry, and for major element and Sr isotope variation in single plagioclase crystals by Chadwick *et al.* (2007) and references therein. Representative major element

analyses of mineral and glass phases conducted for this study are given in **Table 5** and notable micro-textural features of the xenoliths are illustrated in **Fig 10**.

The xenoliths comprise a skarn-type mineral assemblage, dominated by crystallisation of wollastonite and anorthite (up to An<sub>98</sub>). Also present are: diopside, quartz, apatite, sphene, Fe-oxides, calcite, and minor amounts of other calcium-silicate minerals such as grossular garnet, tremolite, larnite, and spurrite. Examination of the xenoliths with the SEM, i.e. on the micron-scale, reveals features which have counterparts in the experimental system.

Vesicular textures are very common within the xenoliths, and are best developed along magma-xenolith contact zones at the hand specimen scale (**Fig 2**). On a finer scale, we observe micro-vesiculation throughout the samples, lending a sponge-like appearance to the most densely vesiculated zones (**Fig 10 a, b**). Although the xenoliths are thermally metamorphosed and largely re-crystallised, small amounts of CaCO<sub>3</sub> are still preserved in places. Calcium carbonate is also found as inclusions within wollastonite crystals (**Fig 10 c**). Carbonate can be found bordered by a Ca-rich (“hyper calcic”) glassy zone with the composition of spurrite, which is in turn closely associated with larnite (**Fig 10 b**). Ca-enriched glassy regions can also be found forming part of a compositional gradient between wollastonite and nearby larnite (**Fig 10 a, c**).

## **DISCUSSION**

The following discussion focuses on mechanisms of carbonate assimilation and the implications of our experimental results for the magmatic system at Merapi volcano, including both deep and shallow level parts of the system. Much of the discussion focuses on the hydrated experiments as these are considered a more reliable representation of the actual compositions involved in carbonate assimilation by a moderately hydrous basaltic-andesitic magma in nature.

## Mechanisms and timescale of carbonate assimilation

The principle process of carbonate assimilation observed in the experiments is carbonate dissociation, i.e. the breakdown of the  $\text{CaCO}_3$  molecule into its component parts  $\text{CaO}$  and  $\text{CO}_2$ . Transport of the resultant molecules in the experimental charges is governed by diffusion in response to the severe chemical gradient generated by the proximally dissociating carbonate. Carbonate dissociation and the resultant loss of  $\text{CO}_2$  are probably the main controlling factors on assimilation rates and are seen to act extremely rapidly. We can semi-quantitatively constrain the timescale of assimilation in the hydrous experiments. Two assumptions have to be made concerning the onset and the termination of assimilation: 1) Inspection of **Fig 3 f** demonstrates that carbonate dissociation began before the target temperature of  $1200^\circ\text{C}$  was reached. We hence estimate the onset of carbonate assimilation at  $t_d < -60\text{s}$ , based on the rapid rate of carbonate assimilation from  $t_d = 0\text{s}$  to  $t_d = 60\text{s}$ . 2) Carbonate assimilation apparently ceased by  $t_d = 90\text{s}$ . However, in preparation for micro-milling, the experiments were polished further, and exposed a minute amount of residual carbonate deep in the experimental capsule at  $t_d = 300\text{s}$ . We nonetheless set  $t_d = 300\text{s}$  as the time required for assimilation of the limestone cube, assuming that the minute residual carbonate will not impact our timescale beyond error of a few seconds. Bearing these points in mind, assimilation of  $9.75\text{g}$  limestone (average) in  $41.93\text{g}$  of magma (average) requires probably not more than ca.  $330\text{s}$  in total, under these experimental conditions. Note that the Ca-rich glass remains in contact with the carbonate throughout the experiment, and becomes saturated in the dissolving components, which then gives rise to the calcite crystallites found in the Ca-rich zone in some cases. This indicates that carbonate assimilation is to some extent limited by the diffusivity of Ca through the contaminated melt region. In nature, we would expect melt convection to remove the Ca-rich glass from the carbonate reaction interface, which would increase the rate of assimilation by maintaining a large compositional gradient at the boundary between carbonate and the host melt.

*In-situ* melting of the solid carbonate was not identified in the experiments presented here. Intra-carbonate glass, occurring as pools and along fractures within the limestone grain, is calcium silicate in composition, indicating that it formed as a result of a mixture of the carbonate components and the M-94-a-107 silicate melt (i.e. a solution of carbonate in the melt, see **Table 4** for composition). Interestingly, the glass-filled fractures frequently intersect in a triple-junction arrangement (**Fig 8 a, b**), which could indicate grain-boundary melting. Based on the composition of the melt, we suggest that the network of intra-carbonate glass instead represents infiltrating Ca-enriched M-94-a-107 melt intruding the disaggregating and dissociating carbonate that has a polygonal fracture pattern and a set of original mineral cleavages that allow rapid advance of invading magmatic melt. Pure calcium carbonate melts at temperatures in excess of 1300°C at 0.5 GPa (Irving & Wyllie, 1975). However, under magmatic conditions, calcite is prone to dissociating before its melting temperature is reached. We know that this process must begin before the target temperature of 1200°C is reached (i.e. during the experiment heat-up phase) as is evidenced by the presence of a Ca-rich melt at  $t_d = 0$ s. Calcite begins to dissociate around 600°C at atmospheric pressure (e.g. Ar & Doğu, 2001), however, the temperature at which this process begins increases with elevated CO<sub>2</sub> pressure (Stern & Weise, 1969). Pressurising our experiments to 0.5 GPa is probably the reason why some carbonate remains undissolved in the zero-time experiments, even though they were heated to 1200°C. We see that once the carbonate is no longer thermally stable, however, it dissociates extremely rapidly in the experiments, particularly so in the hydrated runs.

Carbonate assimilation results in the generation of compositionally distinct melt domains with strongly contrasting viscosities. We can calculate the melt viscosities using the model of Giordano *et al.* (2008), with T set at 1200°C. The model does not incorporate a pressure component, but this should not affect the viscosity calculations significantly, given that viscosity is only weakly dependent on pressure (Richet & Bottinga, 1995). In addition, the model is not calibrated to calculate viscosities for melts with CaO contents exceeding 26 wt.%. For this reason

we cannot reliably estimate the viscosity of the most Ca-enriched melts in experiment (with CaO in excess of e.g. 34 wt%), but we can use melt compositions from the glass interfacial zone, which are moderately enriched in CaO (up to 24 wt.%) and which will provide some insights into the rheological properties of the contaminated melts. We focus on the hydrous melt composition, and calculate  $\log \eta = 1.37$  Pa s for a composition representative of the Ca-normal melt (experiment 386-19, CaO = 9.75 wt%, **Table 3**) and  $\log \eta = 0.27$  Pa s for a composition representative of a moderately Ca-enriched melt (experiment 376-11, CaO = 24 wt%, **Table 3**). The moderately Ca-enriched melt has a very low viscosity relative to the data set of silicate melt viscosities used to calibrate the model of Giordano *et al.* (2008). This may not be too surprising, considering that carbonatite melts are among the lowest viscosity melts on Earth (Dobson *et al.*, 2006). For example, a  $\text{K}_2\text{Ca}(\text{CO}_3)_2$  melt at 1200°C has  $\log \eta \approx -4$  Pa s (see the extrapolated trend in Fig 5 of Dobson *et al.*, 2006). Note that the  $\text{CO}_2$  content of the experimental melts is not taken into account when calculating viscosity because a) it is not incorporated in the Giordano *et al.* (2008) model and b) it has not been measured in our experimental melts. As the effect of dissolved  $\text{CO}_2$  on silicate melt viscosity is qualitatively similar to  $\text{H}_2\text{O}$  (Bourgue & Richet, 2001), we expect that the experimental melts will, in fact, be less viscous than the calculations suggest. In either case, the relatively low viscosity of the Ca-rich melt has implications for some geochemical features of the experiments. For instance, the CaO ‘pile-up’ at the glass interfaces (**Fig 7**) may be a function of contrasting melt viscosities, with CaO accumulating where it reaches a rheological barrier (the Ca-normal glass) that inhibits or slows diffusion. The extent of the contaminated glass is, in turn, dependent on the rate of e.g. Ca (and also Sr) diffusion away from the carbonate and its ability to overcome this barrier. What we see in the experimental products is a “frozen in” CaO (and Sr) pile up effect against such a rheological barrier.

The duration of the experiments is too short for complete homogenisation of the melts to occur. We observe the onset of physical magma mixing (mingling) in localised regions of the

experimental charge (e.g. **Fig 8 d**), probably as a consequence of the differencing melt viscosities and/or compositional convection. Widely contrasting viscosities between melts can hinder the chemical mixing process (e.g. Watson & Jurewicz, 1984; Grasset & Albarède, 1994; Poli *et al.*, 1996; Troll *et al.*, 2004), which would explain the mingled melt domains over distances of up to ca. 100  $\mu\text{m}$  in the experiments. Minor amounts of compositional convection (e.g. Seedhouse & Donaldson, 1996) may also give rise to the mingled textures and may be an additional mechanism of mass transport. The major interactive process between the melts, however, is chemical mixing by interdiffusion. This is evidenced by diffuse mixing zones between the melts over a range of distances from ca. 80 to 450  $\mu\text{m}$  (**Fig 4**). Given sufficient time, the melts will mix fully, despite their contrasting viscosities. This is supported by plotting the composition of the CaO-rich melt in the ternary system  $(\text{Na}_2\text{O})-(\text{Al}_2\text{O}_3+\text{SiO}_2)-(\text{CaO})$  (Lee & Wyllie, 1998), where it falls outside the miscibility gap. The efficacy of mixing is hence time-dependent in the experiments, with mixing zones at their widest in the long dwell time experiments (i.e. ca. 450 $\mu\text{m}$  wide at 300s versus ca. 80 $\mu\text{m}$  wide at 0s, **Fig 4**).

Mixing is also reflected in the Sr isotope systematics of the melts. The  $^{87}\text{Sr}/^{86}\text{Sr}$  profiles fit the CaO profiles well (Fig 5), hence they are well correlated with the major index of contamination in the experiments (i.e. CaO). When placed in a regional context, the contaminated experimental glass overlaps the upper  $^{87}\text{Sr}/^{86}\text{Sr}$  range for Merapi feldspars and is displaced from the Merapi basalt range towards crustal values (**Fig 6**). This supports a carbonate assimilation origin for the radiogenic, crustally contaminated zones in Merapi feldspar. When plotted on a binary mixing line (**Fig 6 b**), the Sr isotopes exhibit a similar feature to that shown in **Fig 7** (Ca pile-up plot), with the most contaminated samples deviating from the mixing line. Furthermore, the longer dwell time experiment demonstrates a greater degree of mixing than the short dwell time experiment. This is consistent with the observations made on the major element profiles, whose interfacial mixing zones increase in length with time. It can be seen from a comparison of the mixing plots (**Fig 6 b**

and 7) that the most contaminated glass in the 300s experiment is a mixture of ca. 40-45% carbonate derived  $^{87}\text{Sr}/^{86}\text{Sr}$  but only ca. 30% carbonate-derived CaO, probably indicating somewhat different rates of transport of Ca versus Sr in experiment.

### ***Pressure effects on the de-carbonation reaction***

The experiments so far discussed have been carried out at 0.5 GPa, simulating a mid to deep crustal magma chamber. To test for pressure effects on the de-carbonation reaction we carried out a hydrous experiment at  $P = 1$  GPa and  $t_d = 300\text{s}$  (**Fig 9**). With respect to major textural features, the 1 GPa experiment is consistent with equivalent experiments run at 0.5 GPa. Vesicles produced at 1 GPa obtain a maximum width of 1.97 mm, which is the same order of magnitude as the maximum vesicle width measured at 0.5 GPa of 1.39 mm, however, there were fewer vesicles present, explaining the slightly larger size in the 1 GPa experiment by simple coalescence. The outcomes of the 1 GPa experiment thus suggests that pressure is not a major influence on the carbonate dissociation reaction in the pressure range  $0.5 < P < 1$  GPa, and that increasing the pressure in the system will cause no perceivable change in the experimental result. Pressure effects may, however, occupy a more important role in a shallower system such as the upper parts of the inter-connected magmatic system beneath Merapi or in the volcanic conduit. Although we could not directly test the effect of lower pressure on the de-carbonation process, we expect that  $\text{CO}_2$  exsolution from the melt will be considerably more vigorous than that observed at 0.5 GPa given that  $\text{CO}_2$  solubility in silicate melts exhibits a positive pressure dependence (Sparks *et al.*, 1994 and references therein). Moreover, a basalt magma at 0.5 GPa and 1200 to 1400°C can dissolve less than 1 wt%  $\text{CO}_2$  (Blank & Brooker, 1994). Decreasing the pressure in our experimental system will thus cause an additional <1 wt.%  $\text{CO}_2$  to exsolve from the basaltic-andesite magma. This is minor in comparison to the large amount of  $\text{CO}_2$  liberated from the carbonate dissociation reaction.

Decompression experiments in which carbonate-bearing mantle xenoliths were brought from 2.5 GPa to 1.0 GPa demonstrate that carbonate dissociates rapidly on decompression, effectively

liberating its CO<sub>2</sub> component (Canil, 1990). We can hence infer that in the high-level parts of the Merapi magmatic system, limestone will be unstable and the decarbonation reaction will proceed at an even higher rate than in our 0.5 GPa experiments. The increased instability of carbonate under these (shallow) conditions may drive sudden over-pressurisation of the upper most parts of the system, and furthermore, if carbonate xenoliths are carried through the conduit on eruption, the effect of decompression may severely intensify volcanic explosions.

## **Implications for the deep-seated system at Merapi**

### ***Contamination via a crustal melt phase***

Calcium contamination of the starting M-94-a-107 basaltic–andesite melt is a ubiquitous feature of the experimental products. Carbonate assimilation results in a Ca-enriched, desilicified, and highly radiogenic strontium melt phase that is in diffusive contact with the normal, starting-composition melt. Evidence of a calc-silicate contaminant melt in the Merapi system can be found in the calc-silicate xenoliths and high-Ca, high <sup>87</sup>Sr/<sup>86</sup>Sr, feldspar zones. However, the natural system being more complex, we can expect that the occurrence of SiO<sub>2</sub> in carbonates (e.g. in ‘dirty’ or silicic limestones) plus a high Si activity in the magma will promote crystallisation of calc-silicate minerals such as wollastonite, spurrite, and larnite along with generation of a CO<sub>2</sub> volatile phase. Such products of carbonate assimilation are found intimately associated in the natural Merapi xenoliths studied: a) carbonate inclusions are found in wollastonite (**Fig 7 c**), b) wollastonite is found mantled by a ‘hyper-calcic’ glass, forming a compositional gradient between the wollastonite and nearby larnite (**Fig 7 b**), c) carbonate is found bordered by a glass zone with the composition of spurrite, which is in turn bordered by larnite (**Fig 7 c**), and d) vesicles recording carbonate degassing are present throughout the xenoliths (**Fig 2**). We should bear in mind that many of the xenoliths represent the ‘end-products’ of magma-carbonate interaction in nature (or near end-products, depending on their residence time), but they nonetheless contain a record that resembles



our experimental products. Model mineral stability fields have been calculated using THERMOCALC (Powell & Holland, 1988). With pressure set at 0.2 GPa (shallow system), wollastonite is the first stable phase following reaction between calcium carbonate and available silica in the presence of a CO<sub>2</sub>-bearing fluid at ca. 600°C. With increasing temperature (and/or addition of water), spurrite followed by larnite will stabilise, also following reaction of calcium carbonate and silica, thus verifying the paragenesis inferred from the xenoliths. Note that increasing the pressure in the model serves to increase the temperature at which the various phases are stable. For the deeper parts of the Merapi system, the Ca-rich melt in experiment is hence interpreted as a precursor to the “hyper calcic” phases in the xenoliths, i.e. spurrite and larnite.

A consideration of all of the experimental data reinforces this point. In **Fig 11** we see a progressive enrichment of the starting material with the limestone-derived CaO. The glass analyses plotted represent all of the time stages of carbonate assimilation studied, and demonstrates how carbonate assimilation progresses and causes the contaminant melt to evolve towards the composition of the ‘hyper calcic’ contaminated regions in the calc-silicate xenoliths. This is strong evidence for the presence of on-going, progressive carbonate assimilation at Merapi volcano and for contamination via a carbonated, extremely calcic melt phase. Limestone contamination in this manner has also been suggested for other settings, such as the Hortavaer igneous complex in Norway (Barnes *et al.*, 2005), the Colli Albani volcanic district, Italy (Gaeta *et al.*, 2009), and Oldoinyo Lengai volcano, Tanzania (Mitchell, 2009).

### ***Effect of a mobile calcic melt on the magma system***

Due to their relatively low viscosities, carbonated melts are highly mobile, thus enhancing their ability to migrate through a partially crystallised magma body and possibly even mobilise semi-arrested regions of the magma system. In the deeper parts of the Merapi system, this process could aid mixing between magma pockets (e.g. Nakagawa *et al.*, 2002) and enable recycling of

phenocrysts (e.g. Charlier *et al.*, 2005). The relatively mobile Ca-rich, high  $^{87}\text{Sr}/^{86}\text{Sr}$  melt will then be able to contaminate local regions of the system, by convective mixing and/or diffusion.

The rheology of the melt also has implications for bubble growth over relatively short length scales. The Ca-rich melt phase gives rise to the largest bubbles, which is probably a function of its relatively low viscosity. This type of melt offers less resistance for bubble expansion and coalescence. Moreover, the Ca-rich zone is locally  $\text{CO}_2$  super-saturated, due to the proximally decomposing carbonate, favouring additional bubble growth and enlargement.

### **Implications for the shallow system at Merapi**

#### ***The volatile budget***

Volatile exsolution from the experimental melts, and associated vesiculation, reaches a maximum in the Ca-rich glass, and is observed at all time intervals of magma-carbonate interaction. Water solubility in a basalt at  $1200^\circ\text{C}$  and 0.5 GPa is ca. 8.5 wt.% (e.g. VolatileCalc, Newman & Lowenstern, 2002). However, adding  $\text{CO}_2$  to the system through carbonate dissolution causes a significant drop in  $\text{H}_2\text{O}$  melt solubility (Botcharnikov *et al.*, 2005). Hence, the vesicles in experiment may be due to exsolution of both  $\text{CO}_2$  and  $\text{H}_2\text{O}$ , with  $\text{CO}_2$  being the most abundant volatile. As ca. 0.4 wt.%  $\text{CO}_2$  is soluble in the basaltic-andesite starting material (e.g. King & Holloway, 2002), most of the  $\text{CO}_2$  added to the system through carbonate assimilation is expected to be present as an exsolved volatile phase. We can hence calculate that an average of ca. 4.3 mg of  $\text{CO}_2$  is liberated in the experiments, which occupies ca. 7 vol.% of the experimental capsule. If we consider assimilation in nature of a limestone cube with 80m side length, ca.  $5.6 \times 10^5$  tonnes of  $\text{CO}_2$  will be produced. Given the short timescale of carbonate assimilation observed in the experiments, it is wholly conceivable that up to  $5.6 \times 10^5$  tonnes of  $\text{CO}_2$  can be generated over a period of two weeks by carbonate assimilation alone. For instance, limestone assimilation and

associated CO<sub>2</sub> release of this scale ( $5.4 \times 10^5$  tonnes of CO<sub>2</sub> over 17 days) has been inferred for Popocatepetl volcano in Mexico based on measured excess CO<sub>2</sub> emissions (Goff *et al.*, 2001).

Models of CO<sub>2</sub> provenance and fluxes at oceanic arcs generally do not take the arc crust into account as a potential volatile source (e.g. Hilton *et al.*, 2002). For example, the proportion of the components of arc contributions to the global CO<sub>2</sub> flux is estimated at 10-15% from the mantle wedge and 85-90% from decarbonation of subducted carbonate and carbonate-bearing sedimentary rocks (after Hilton *et al.*, 2002 and references therein). The experiments presented here show that CO<sub>2</sub> liberated from carbonate-rich lithologies in the arc crust can constitute a significant contribution to the volatile budget at subduction zones (with ca. 32,000 t/day of excess CO<sub>2</sub> being realistic, *cf.* Goff *et al.*, 2001). Such late-stage CO<sub>2</sub> fluxes are probably highly variable over long time-scales, but, on the short term, de-carbonation of limestone can produce substantial amounts of crustal CO<sub>2</sub> and should be considered when investigating and modelling volcanic volatile budgets.

### ***Crustal de-carbonation as an eruption trigger?***

Carbon dioxide gas liberation as a result of limestone assimilation at mid to shallow crustal depths in the Merapi magmatic system may have serious implications for the eruptive dynamics of this high-risk volcano. Intense episodes of carbonate de-volatilisation within the mid to upper crust has the potential to over-pressurise the magmatic system over short timescales (hours to days), which may lead to an eruptive event with very limited forewarning. Although carbonate assimilation is probably an on-going process at Merapi, its potential to act as an eruption trigger could be magnified if external forcing, such as an earthquake, were to act on the system. A case in point is the major 2006 Yogyakarta earthquake ( $M = 6.4$ , Walter *et al.*, 2008), which coincided with activity at Merapi. The event was followed by an up to 3-fold increase in dome growth and dome collapse activity for a period of 16 days after the earthquake (Harris & Ripepe, 2007; Walter *et al.*, 2007). We speculate that stress changes and shaking in the mid to upper crust due to seismic waves associated with the earthquake may have shaken up and fractured the crustal limestone units

underlying Merapi, resulting in vigorous release of trapped bubbles and renewed crustal de-carbonation due to an increase in limestone surface area available to react with the magma. Decomposition of CO<sub>2</sub>-bearing xenoliths in this way is a much more efficient contamination mechanism than by wall-rock interaction alone (e.g. Watson *et al.*, 1982; Freda *et al.*, 2008b). This additional CO<sub>2</sub> release, potentially of the order 32,000 t/day (*cf.* Goff *et al.*, 2001), would have rapidly increased the CO<sub>2</sub> pressure in the system, promoting increased eruptive activity following the 2006 earthquake. The risk of such intensified episodes of carbonate de-volatilisation at Merapi has serious repercussions for hazard mitigation, which will need to be sufficiently flexible to cope with an eruptive crisis when given potentially very little forewarning. This would also apply to other volcanic systems emplaced within carbonate crust, that may likewise be susceptible to overpressurisation following vigorous reaction between magma and limestone, e.g. Popocatepetl, Mexico and Vesuvius, Italy, both of which have a record of sustained explosive activity.

## **SUMMARY**

The time-constrained series of short duration experiments presented here provides a thus far unique opportunity to observe the textural, chemical, and isotopic interaction between magma and carbonate crust as carbonate assimilation proceeds. The major features of carbonate assimilation identified are: i) rapid decomposition and degassing of carbonate, ii) generation of a relatively low viscosity, calcic, high <sup>87</sup>Sr/<sup>86</sup>Sr contaminant melt, iii) local CO<sub>2</sub> volatile super-saturation and subsequent vigorous bubble growth within the affected region, iv) physical mingling between the contaminated and unaffected melt domains, and v) chemical mixing between melts.

Considering the experimental data in conjunction with the existing petrological, mineral, and geochemical data for Merapi (e.g. Gertisser & Keller, 2003; Chadwick *et al.*, 2007), we can verify that intra-crustal to late-stage carbonate assimilation and associated volatile degassing are significant magma-chamber processes that affect mineral composition, magma evolution, and

potentially eruptive behaviour at Merapi volcano. In light of this realisation, the volatile budget at Merapi demands a re-evaluation to take into account late-stage, intra-crustal de-carbonation events.

## **ACKNOWLEDGEMENTS**

We are grateful to L.M. Schwarzkopf for providing sample material, H. Behrens for producing the hydrated glass and for KFT analysis, S. Mollo for producing the anhydrous glass, A. Cavallo for microprobe technical assistance and support at INGV, J. Malarkey for micromilling technical support, and Chris Ottley and Geoff Nowell respectively at NCIET Durham for assistance with elemental and isotopic analysis of the microsamples. FMD is grateful to S. and E. Vinciguerra for their hospitality during this work. A. Skelton, O. Spieler, J. Blundy, and J. Taddeucci are thanked for stimulating and encouraging discussion. We are grateful to C. Barnes, F. Ridolfi, and one anonymous reviewer for their thorough and thoughtful reviews which helped to greatly improve the manuscript. This work was supported by the Swedish Science Foundation (Vetenskapsrådet) grant number 621-2007-5028 to VRT and by Project FIRB MIUR “Development of innovative technologies for the environmental protection from natural events”.

## **REFERENCES**

- Abratis, M., Schmincke, H.-U. & Hansteen, T.H. (2002). Composition and evolution of submarine volcanic rocks from the central and western Canary Islands. *International Journal of Earth Sciences (Geol Rundsch)* **91**, 562-582.
- Abdurachman, E.K., Bourdier, J.-L. & Voight, B. (2000). Nuées ardentes of 22 November 1994 at Merapi volcano, Java, Indonesia. *Journal of Volcanology and Geothermal Research* **100**, 345-361.
- Annen, C. & Sparks, R.S.J. (2002). Effects of repetitive emplacement of basaltic intrusions on thermal evolution and melt generation in the crust. *Earth and Planetary Science Letters* **203**, 937-955.

- Ar, I. & Doğu, G. (2001). Calcination kinetics of high purity limestones. *Chemical Engineering Journal* **83**, 131-137.
- Barnes, C.G., Prestvik, T., Sundvoll, B. & Surratt, D. (2005). Pervasive assimilation of carbonate and silicate rocks in the Hortavaer igneous complex, north-central Norway. *Lithos* **80**, 179-199.
- Beard, J.S., Abitz, R.J. & Lofgren, G.E. (1993). Experimental melting of crustal xenoliths from Kilbourne Hole, new Mexico and implications for the contamination and genesis of magmas. *Contributions to Mineralogy and Petrology* **115**, 88-102.
- Behrens, H., (1995). Determination of water solubilities in high-viscosity silicate glasses: An experimental study on NaAlSi<sub>3</sub>O<sub>8</sub> and KAlSi<sub>3</sub>O<sub>8</sub> melts. *European Journal of Mineralogy* **7**, 905–920.
- Blank, J.G. & Brooker, R.A. (1994). Experimental studies of carbon dioxide in silicate melts: solubility, speciation, and stable carbon isotope behavior. In: Carroll, M.R. & Holloway, J.R. (eds.) *Volatiles in Magmas. Mineralogical Society of America, Reviews in Mineralogy* **30**, 157-186.
- Botcharnikov, R., Freise, M., Holtz, F. & Behrens, H. (2005). Solubility of C-O-H mixtures in natural melts: new experimental data and application range of recent models. *Annals of Geophysics* **48**, 633-646.
- Bourgue, E. & Richet, P. (2001). The effects of dissolved CO<sub>2</sub> on the density and viscosity of silicate melts: a preliminary study. *Earth and Planetary Science Letters* **193**, 57-68.
- Camus, G., Gourgaud, A., Mossand-Berthommier, P.-C. & Vincent, P.-M. (2000). Merapi (Central Java, Indonesia): An outline of the structural and magmatological evolution, with a special emphasis to the major pyroclastic events. *Journal of Volcanology and Geothermal Research* **100**, 139-163.

- Canil, D. (1990). Experimental study bearing on the absence of carbonate in mantle-derived xenoliths. *Geology* **18**, 1011-1013.
- Chadwick, J.P., Troll, V.R., Ginibre, C., Morgan, D., Gertisser, R., Waight, T.E. & Davidson, J.P. (2007). Carbonate assimilation at Merapi volcano, Java, Indonesia: Insights from crystal isotope stratigraphy. *Journal of Petrology* **48**, 1793-1812.
- Chadwick, J.P. (2008). Magma crust interaction in volcanic systems: Case studies from Merapi Volcano, Indonesia, Taupo Volcanic Zone, New Zealand, and Slieve Gullion, N.Ireland. PhD thesis, Trinity College Dublin, Ireland. p. 52-181.
- Charbonnier, S.J. & Gertisser, R. (2008). Field observations and surface characteristics of pristine block-and-ash flow deposits from the 2006 eruption of Merapi Volcano, Java, Indonesia. *Journal of Volcanology and Geothermal Research* **177**, 971-982.
- Charlier, B.L.A., Wilson, C.J.N., Lowenstern, J.B., Blake, S., Van Calsteren, P.W. & Davidson, J.P. (2005). Magma generation at a large, hyperactive silicic volcano (Taupo, New Zealand) revealed by U-Th and U-Pb systematic in zircons. *Journal of Petrology* **46**, 3-32.
- Charlier, B.L.A., Ginibre, C., Morgan, D., Nowell, G.M., Pearson, D.G., Davidson, J.P. & Ottley, C.J. (2006). Methods for microsampling and high-precision analysis of strontium and rubidium isotopes at single crystal scale for petrological and geochronological applications. *Chemical Geology* **232**, 114-133.
- Clochiatti, R., Joron, J.L., Kerinec, F. & Treuil, M. (1982). Quelques données préliminaires sur la lave du dome actuel du volcan Merapi (Java Indonésie) et sur ses enclaves. *Comptes Rendus de l'Académie des Sciences, Série A* **295**, 817-822.
- Curray, J.R., Shor, G.G., Raitt, R.W. & Henry, M. (1977). Seismic refraction and reflection studies of crustal structure of the Eastern Sunda and Western Banda arcs. *Journal of Geophysical Research* **82**, 2479-2489.

- Dallai, L., Freda, C. & Gaeta, M. (2004). Oxygen isotope geochemistry of pyroclastic clinopyroxene monitors carbonate contributions to Roman-type ultrapotassic magmas. *Contributions to Mineralogy and Petrology* **148**, 247-263.
- Davidson, J.P., Hora, J.M., Garrison, J.M. & Dungan, M.A. (2005). Crustal forensics in arc magmas. *Journal of Volcanology and Geothermal Research* **140**, 157-170.
- de Genevraye, P. & Samuel, L. (1972). Geology of the Kendang Zone (Central and East Java). *Proceedings, First Annual Convention, Indonesian Petroleum Association*, pp. 17-30.
- Del Moro, A., Fulignati, P., Marianelli, P., & Sbrana, A. (2001). Magma contamination by direct wall rock interaction: constraints from xenoliths from the walls of a carbonate-hosted magma chamber (Vesuvius 1944 eruption). *Journal of Volcanology and Geothermal Research* **112**, 15-24.
- Dobson, D.P., Jones, A.P., Rabe, R., Sekine, T., Kurita, K., Taniguchi, T., Kondo, T., Kato, T., Shimomura, O. & Urakawa, S. (1996). In-situ measurement of viscosity and density of carbonate melts at high pressure. *Earth and Planetary Science Letters* **143**, 207-215.
- Donoghue, E., Troll, V.R., Schwarzkopf, L.M., Clayton, G. & Goodhue, R. (2009). Organic block coatings in block-and-ash flow deposits at Merapi Volcano, central Java. *Geological Magazine* **146**, 113-120.
- Font, L., Davidson, J.P., Pearson, D.G., Nowell, G.M., Jerram, D.A. & Ottley, C.J. (2008). Sr and Pb isotope micro-analysis of plagioclase crystals from Skye lavas: an insight into open-system processes in a flood basalt province. *Journal of Petrology* **49**, 1449-1471.
- Freda, C. & Baker, D.R. (1998). Na-K interdiffusion in alkali feldspar melts. *Geochimica et Cosmochimica Acta* **62**, 2997-3007.
- Freda, C., Gaeta, M., Palladino, D.M. & Trigila, R. (1997). The Villa Senni Eruption (Alban Hills, central Italy): the role of H<sub>2</sub>O and CO<sub>2</sub> on the magma chamber evolution and on the eruptive scenario. *Journal of Volcanology and Geothermal Research* **78**, 103-120.



- Freda, C., Baker, D.R. & Ottolini, L. (2001). Reduction of water loss from gold-palladium capsules during piston cylinder experiments by use of pyrophyllite powder. *American Mineralogist* **86**, 234-237.
- Freda, C., Gaeta, M., Misiti, V., Mollo, S., Dolfi, D. & Scarlato, P. (2008a). Magma-carbonate interaction: An experimental study on ultrapotassic rocks from Alban Hills (Central Italy). *Lithos* **101**, 397-415.
- Freda, C., Gaeta, M., Giaccio, B., Marra, F., Palladino, D.M., Scarlato, P. & Sottili, G. (2008b). Magma-country rock interaction during large mafic explosive eruptions: evidence from Colli Albani (Central Italy). In: *Abstracts, 33<sup>rd</sup> IGC 2008 Oslo, Norway (2008)*.
- Fulignati, P., Marianeli, P., Santacroce, R. & Sbrana, A. (2004). Probing the Vesuvius magma chamber-host rock interface through xenoliths. *Geological Magazine* **141**, 417-428.
- García-Moreno, O., Castro, A., Corretgé, L.G. & El-Hmidi, H. (2006). Dissolution of tonalitic enclaves in ascending hydrous granitic magmas: An experimental study. *Lithos* **89**, 245-258.
- Gaeta, M., Di Rocco, T. & Freda, C. (2009). Carbonate assimilation in open magmatic systems: the role of melt-bearing skarns and cumulate forming processes. *Journal of Petrology* **50**, 361-385.
- Gasparon, M., Hilton, D.R. & Varne, R. (1994). Crustal contamination processes traced by helium isotopes: Examples from the Sunda arc, Indonesia. *Earth and Planetary Science Letters* **126**, 15-22.
- Gasparon, M. & Varne, R. (1998). Crustal assimilation versus subducted sediment input in west Sunda arc volcanics: an evaluation. *Mineralogy and Petrology* **64**, 89-117.
- Gertisser, R. (2001). Gunung Merapi (Java, Indonesien): Eruptionsgeschichte und magmatische Evolution eines Hochrisiko-Vulkans. PhD thesis, Universität Freiburg.
- Gertisser, R. & Keller, J. (2003). Trace elements and Sr, Nd, Pb and O isotope variations in medium-K and high-K volcanic rocks from Merapi Volcano, Central Java, Indonesia:

- Evidence for the involvement of subducted sediments in Sunda arc magma genesis. *Journal of Petrology* **44**, 457-489.
- Gilg, H.A., Lima, A., Somma, R., Belkin, H.E., De Vivo, B. & Ayuso, R.A. (2001). Isotope geochemistry and fluid inclusion study of skarns from Vesuvius. *Mineralogy and Petrology* **73**, 145-176.
- Giordano, D., Russell, J.K. & Dingwell, D.B. (2008). Viscosity of magmatic liquids: a model. *Earth and Planetary Science Letters* **271**, 123-134.
- Goff, F., Love, S.P., Warren, R.G., Counce, D., Obenholzner, J., Siebe, C. & Schmidt, S.C. (2001). Passive infrared remote sensing evidence for large, intermittent CO<sub>2</sub> emissions at Popocatepetl volcano, Mexico. *Chemical Geology* **177**, 133-156.
- Grasset, O. & Albarède, F. (1994). Hybridization of mingling magmas with different densities. *Earth and Planetary Science Letters* **121**, 327-332.
- Hall, R. (2002). Cenozoic geological and plate tectonic evolution of SE Asia and the SW Pacific: computer-based reconstructions, model and animations. *Journal of Asian Earth Sciences* **20**, 353-431.
- Hamilton, W. (1979). *Tectonics of the Indonesian Region*. US Geological Survey, *Professional Papers* **1078**, 1-345.
- Harris, A.J.L. & Ripepe, M. (2007). Regional earthquakes as a trigger for enhanced volcanic activity: evidence from MODIS thermal data. *Geophysical Research Letters* **34**, LO2304, doi: 10.1029/2006GL028251.
- Hilton, D.R., Fischer, T.P. & Marty, B. (2002). Noble gases and volatile recycling at subduction zones. In: Porcelli, D.P., Ballentine, C.J. & Wieler, R. (eds.) *Noble Gases, Mineralogical Society of America, Reviews in Mineralogy* **47**, 319-370.

- Huang, W.-L., Wyllie, P.J. & Nehru, C.E. (1980). Subsolidus and liquidus phase relationships in the system CaO-SiO<sub>2</sub>-CO<sub>2</sub> to 30 kbar with geological applications. *American Mineralogist* **65**, 285-301.
- Hudon, P., Baker, D.R. & Toft, P.B. (1994). A high-temperature assembly for 1.91 cm (3/4") piston-cylinder apparatus. *American Mineralogist* **79**, 145-147.
- Iacono Marziano, G., Gaillard, F. & Pichavant, M. (2008). Limestone assimilation by basaltic magmas: an experimental re-assessment and application to Italian volcanoes. *Contributions to Mineralogy and Petrology* **155**, 719-738.
- Iezzi, G., Mollo, S., Ventura, G., Cavallo, A. & Romano, C. (2008). Experimental solidification of anhydrous latitic and trachytic melts at different cooling rates: The role of nucleation kinetics. *Chemical Geology* **253**, 91-101.
- Irving, A.J. & Wyllie, P.J. (1975). Subsolidus and melting relationships for calcite, magnesite and the join CaCO<sub>3</sub>-MgCO<sub>3</sub> to 36 kb. *Geochimica et Cosmochimica Acta* **39**, 35-53.
- Johnston, A.D. & Wyllie, P.J. (1988). Interaction of granitic and basic magmas: experimental observations on contamination processes at 10 kbar with H<sub>2</sub>O. *Contributions to Mineralogy and Petrology* **98**, 352-362.
- King, P.L. & Holloway, J.R. (2002). CO<sub>2</sub> solubility and speciation in intermediate (andesitic) melts: The role of H<sub>2</sub>O and composition. *Geochimica et Cosmochimica Acta* **66**, 1627-1640.
- Knesel, K.M. & Davidson, J.P. (2002). Insights into collisional magmatism from isotopic fingerprints of melting reactions. *Science* **296**, 2206-2208.
- Koulakov, I., Bohm, M., Asch, G., Lühr B.-G., Manzanares, A., Brotopuspito, K.S., Fauzi, P., Purbawinata, M.A., Puspito, N.T., Ratdomopurbo, A. Kopp, H., Rabbel, W., Sheykunova, E. (2007). P and S velocity structure of the crust and the upper mantle beneath central Java from local tomography inversion. *Journal of Geophysical Research* **112**, B08310, doi:10.1029/2006JB004712.

- Lee, W.-J. & Wyllie, P.J. (1998). Petrogenesis of carbonatite magmas from mantle to crust, constrained by the system CaO–(MgO + FeO)–(Na<sub>2</sub>O + K<sub>2</sub>O)–(SiO<sub>2</sub> + Al<sub>2</sub>O<sub>3</sub> + TiO<sub>2</sub>)–CO<sub>2</sub>. *Journal of Petrology* **39**, 495-517.
- Macdonald, R., Hawkesworth, C.J. & Heath, E. (2000). The Lesser Antilles volcanic chain: a study in arc magmatism. *Earth Science Reviews* **49**, 1-76.
- Macpherson, C.G., Gamble, J.A. & Matthey, D.P. (1998). Oxygen isotope geochemistry of lavas from an oceanic to continental arc transition, Kermadec–Hikurangi margin, SW Pacific. *Earth and Planetary Science Letters* **160**, 609-621.
- McLeod, P. & Sparks, S.J. (1998). The dynamics of xenoliths assimilation. *Contributions to Mineralogy and Petrology* **132**, 21-33.
- Médard, E., McCammon, C.A., Barr, J.A. & Grove, T.L. (2008). Oxygen fugacity, temperature reproducibility, and H<sub>2</sub>O contents of nominally anhydrous piston-cylinder experiments using graphite capsules. *American Mineralogist* **93**, 1838-1844.
- Misiti, V., Taddeucci, J., Freda, C., Deegan, F., Troll, V. & Blythe, L. (2008). Vesiculation of andesitic melts during carbonate assimilation. In: *Abstracts, 12<sup>th</sup> International Conference on Experimental Mineralogy, Petrology and Geochemistry (EMPG-XII), Innsbruck, Austria (2008)*.
- Mitchell, R.H. (2009). Peralkaline nephelinite-natrocarbonatite immiscibility and carbonate assimilation at Oldoinyo Lengai, Tanzania. *Contributions to Mineralogy and Petrology* **158**, 589-598.
- Mollo, S., Gaeta, M., Freda, C. & Di Rocco, T. (2010). Carbonate assimilation in magmas: A reappraisal based on experimental petrology. *Lithos* **114**, 503-514.
- Nakagawa, M., Wada, K. & Wood, P. (2002). Mixed magmas, mush chambers and eruption triggers: evidence from zoned clinopyroxene phenocrysts in andesitic scoria from the 1995 eruptions of Ruapehu volcano, New Zealand. *Journal of Petrology* **43**, 2279-2303.

- Newman, S. & Lowenstern, J.B. (2002). VolatileCalc: a silicate melt-H<sub>2</sub>O-CO<sub>2</sub> solution model written in Visual Basic for excel. *Computers & Geosciences* **28**, 597-604.
- Poli, G., Tommasini, S. & Halliday, A.N. (1996). Trace element and isotopic exchange during acid-basic magma interaction processes. *Transactions of the Royal Society of Edinburgh: Earth Sciences* **87**, 225-232.
- Powell, R. & Holland, T.J.B. (1988). An internally consistent thermodynamic dataset with uncertainties and correlations: 3. Application to geobarometry, worked examples and a computer program. *Journal of Metamorphic Petrology* **6**, 173-204.
- Richet, P. & Bottinga, Y. (1995). Rheology and configurational entropy of silicate melts. In: Stebbins, J.F., McMillan, P.F. & Dingwell, D.B. (Eds.) *Structure, Dynamics and Properties of Silicate Melts. Mineralogical Society of America, Reviews in Mineralogy and Geochemistry* **32**, 67-93.
- Sachs, P.M. & Strange, S. (1993). Fast assimilation of xenoliths in magmas. *Journal of Geophysical Research* **98**, 19741-19754.
- Schaaf, P., Stimac, J., Siebe, C. & Macias, J. L. (2005). Geochemical evidence for mantle origin and crustal processes in volcanic rocks from Popocatépetl and surrounding monogenetic volcanoes, Central Mexico. *Journal of Petrology* **46**, 1243-1282.
- Schwarzkopf, L.M., Schmincke, H.-U. & Troll, V.R. (2001). Pseudotachylite on impact marks of block surfaces in block-and-ash flows at Merapi volcano, Central Java, Indonesia. *International Journal of Earth Sciences (Geol Rundsch)* **90**, 769-775.
- Schwarzkopf, L.M., Schmincke, H.-U. & Cronin, S.J. (2005). A conceptual model for block-and-ash flow basal avalanche transport and deposition, based on deposit architecture of 1998 and 1994 Merapi flows. *Journal of Volcanology and Geothermal Research* **139**, 117-134.
- Seedhouse, J.K. & Donaldson, C.H. (1996). Compositional convection caused by olivine crystallization in a synthetic basalt melt. *Mineralogical Magazine* **60**, 115-130.

- Smith, T.E., Thirlwall, M.F. & Macpherson, C. (1996). Trace element and isotopic geochemistry of the volcanic rocks of Bequia, Grenadine Islands, lesser Antilles Arc: a study of subduction enrichment and intra-crustal contamination. *Journal of Petrology* **37**, 117-143.
- Smith, I.E.M., Worthington, T.J., Price, R.C., Stewart, R.B. & Maas, R. (2006). Petrogenesis of dacite in an oceanic subduction environment: Raoul Island, Kermadec arc. *Journal of Volcanology and Geothermal Research* **156**, 252-265.
- Smyth, H.R., Hall, R., Hamilton, J. & Kinny, P. (2005). East Java: Cenozoic Basins, Volcanoes and Ancient Basement. *Proceedings, Indonesian Petroleum Association, Thirtieth Annual Convention & Exhibition*.
- Smyth, H.R., Hamilton, P.J., Hall, R. & Kinny, P.D. (2007). The deep crust beneath island arcs: Inherited zircons reveal a Gondwana continental fragment beneath East Java, Indonesia. *Earth and Planetary Science Letters* **258**, 269-282.
- Sparks, R.S.J., Barclay, J., Jaupart, H.M. & Philips, J.C. (1994). Physical aspects of magma degassing 1: Experimental and theoretical constraints on vesiculation. In: Carroll, M.R. & Holloway, J.R. (eds.) *Volatiles in Magmas, Mineralogical Society of America, Reviews in Mineralogy* **30**, 413-445.
- Stern, K.H. & Weise, E.L. (1969). High temperature properties and decomposition of inorganic salts. Part2: Carbonates. *National Standard Reference Data System, National Bureau of Standards (U.S.)* **30**, 32pp.
- Troll, V. R., Schwarzkopf, L. M., Gertisser, R., Buckley, C., Chadwick, J., Zimmer, M. & Sulistiyo, Y. (2003). Shallow-level processes and their impact on the eruptive behaviour in arc volcanoes: evidence from recent Merapi lavas. In: *Abstracts, State of the Arc Meeting, Portland, Oregon (2003)*.

- Troll, V.R., Donaldson, C.H. & Emeleus, C.H. (2004). Pre-eruptive magma mixing in ash-flow deposits of the Tertiary Rum Igneous Centre, Scotland. *Contributions to Mineralogy and Petrology* **147**, 722-739.
- Untung, M. & Sato, Y. (1978). Gravity and Geological studies in Java, Indonesia. *Geological Survey of Indonesia and Geological Survey of Japan, Special Publication* **6**, 207 pp.
- van Bemmelen, R. W. (1949). *The Geology of Indonesia, 1A, General Geology*. The Hague: Government Printing Office.
- Voight, B., Constantine, E.K., Siswowardjyo, S. & Torley, R. (2000). Historical eruptions of Merapi volcano, Central Java, Indonesia, 1768-1998. *Journal of Volcanology and Geothermal Research* **100**, 69-138.
- Wagner, D., Koulakov, I., Rabbel, W., Luehr, B.-G., Wittwer, A., Kopp, H., Bohm, M., Asch, G. and the MERAMEX Scientists (2007). Joint inversion of active and passive seismic data in Central Java. *Geophysical Journal International* **170**, 923-932.
- Walter, T.R., Wang, R., Zimmer, M., Grosser, H., Lühr, B. & Ratdomopurbo, A. (2007). Volcanic activity influenced by tectonic earthquakes: static and dynamic stress triggering at Mt. Merapi. *Geophysical Research Letters* **34**, L05304, doi:10.1029/2006GL028710.
- Walter, T.R., Wang, R., Luehr, B.-G., Wassermann, J., Behr, Y., Parolai, S., Anggraini, A., Günther, E., Sobiesiak, M., Grosser, H., Wetzel, H.-U., Milkereit, C., Sri Brotopuspito, P. J. K., Harjadi, P. & Zschau, J. (2008). The 26 May 2006 magnitude 6.4 Yogyakarta earthquake south of Mt. Merapi volcano: Did lahar deposits amplify ground shaking and thus lead to the disaster? *Geochemistry, Geophysics, Geosystems* **9**, doi: 10.1029/2007GC001810.
- Watson, E.B. (1982). Basalt contamination by continental crust: some experiments and models. *Contributions to Mineralogy and Petrology* **80**, 73-87.
- Watson, E.B., Sneeringer, M.A. & Ross, A. (1982). Dissolution of dissolved carbonate in magmas: experimental results and applications. *Earth and Planetary Science Letters* **61**, 346-358.

Watson, E.B. & Jurewicz, S.R. (1984). Behavior of alkalies during diffusive interaction of granitic xenoliths with basaltic magma. *The Journal of Geology* **92**, 121-131.



## FIGURE CAPTIONS

**Figure 1 a:** Overview map of the Sunda arc, Indonesia. Unfilled circles represent volcanic centres; Merapi volcano (Central Java) is labelled. Cross hatched area is Mesozoic continental crust (Sundaland), which probably extends as far as Central Java. Map is modified after Gertisser and Keller (2003) using crustal boundaries in Smyth et al (2007) and references therein. **1 b:** Simplified map of the area surrounding Merapi and Merbabu volcanoes (corresponds to the box in Figure 1 a), showing the major geologic zones bounding the Central Volcanic Zone (see text for further explanation). Sample locations for this study are indicated (1998 and 1994 xenolith-bearing block and ash flows (BAF) on the S flanks of Merapi and the limestone sample site at Parangtritis beach, coast S of Merapi). Significant population centres in the vicinity of Merapi are also shown, the largest of which is Yogyakarta ca. 25 - 30km to the south. **1 c:** Schematic section through the crust and mantle beneath Merapi to 50km, showing an interconnected network of magma chambers beneath the volcano. Sketch is modified after Chadwick (2008), based on a combination of 3D seismic tomography and pyroxene + amphibole barometry data (see text for details).

**Figure 2:** Representative examples of Merapi calc-silicate xenoliths (xcs) from a 1998 block and ash flow (for map location see **Fig 1 b**) at hand-specimen scale. Samples display intensely developed xenolith-magma contact zones with vesicular textures and skarn-type mineral assemblages. Mineral abbreviations: Wo = wollastonite, Di = diopside, An = anorthite, Qz = quartz. Mineral assemblages listed in figure are in order of decreasing abundance.

**Figure 3:** BSE images of the experimental products arranged to show the temporal sequence and major textural features of magma-carbonate interaction in the experiments. The anhydrous (**3 a-e**) and hydrous (**3 f-j**) experimental series are shown in the left and right columns, respectively. All experiments were carried out at  $T = 1200^{\circ}\text{C}$  and  $P = 0.5 \text{ GPa}$ . The Ca-rich and Ca-normal glass domains can be distinguished by their contrasting brightness in the images, where the bright glass is

Ca-rich and the dark grey glass is Ca-normal. Thick white lines on (f), (h), and (j) are EMPA lines, corresponding to the graphs in **Fig. 4**.

**Figure 4:** Representative major and minor element chemical profiles in hydrated runs at 0s (a, d), 90s (b, e), and 300s (c, f), respectively. Profiles correspond to thick white EMPA lines in **Fig 3 f, h, j**. The glass interfacial region is highlighted with grey shading on the plots. This is the region spanning the Ca-enriched melt-Ca-normal melt contact over which a steady interchange between CaO and SiO<sub>2</sub> is observed. Note that the glass interfacial region is considerably wider at 300s (ca. 450µm max) than at 0s and 90s (ca. 80µm max for both).

**Figure 5:** <sup>87</sup>Sr/<sup>86</sup>Sr and CaO wt% profiles in (a) a 0s experiment (379-17) and (b) a 300s experiment (386-19). Drilled areas are highlighted in grey on the BSE images (taken prior to mounting for drilling), and correspond to the numbered rectangles on the plot. The length of the rectangles corresponds to the area drilled and their height includes ±2 SE. Grey shaded vertical bars represent the glass interfacial regions.

**Figure 6:** (a) <sup>87</sup>Sr/<sup>86</sup>Sr values for Merapi basalts, feldspars, crustal xenoliths, and local crust, (compiled using data in Gertisser & Keller (2003) and Chadwick *et al.* (2007)) relative to experimental glass (this study). Note that the uncontaminated glass is within the range of recent Merapi basalts, while by contrast, the Ca-enriched glass is displaced towards crustal values. (b) <sup>87</sup>Sr/<sup>86</sup>Sr binary mixing model between the end-members used in experiment (the mixing line is straight because 1/Sr is used). Composition of the drilled samples of experimental glass have been affected by between 10 and 45% limestone-derived Sr. Note that the longer dwell time experiment (300s) exhibits the greatest degree of mixing (45%). Samples from the most severely contaminated regions in both experiments (drill areas 3 in Fig 5) are displaced from the mixing line (labelled as “samples of Ca-rich glass” on the plot). See also Figure 7.

**Figure 7:** Experiment 386-19 with microprobe analysis line through the intra-glass interface shown with a thick white line (**5 a**). All points from this traverse (n = 59) are normalised to 100% and

plotted on a binary mixing line between the starting compositions used in experiment, also normalised to 100% (**5 b**). Notice that at the low SiO<sub>2</sub> range, the data closely fits the mixing line, whereas towards the Ca-normal glass composition the data indicates slight CaO enrichment. This feature is interpreted as a pile-up of Ca at the Ca-normal glass interface (see discussion).

**Figure 8:** Fine scale textural features of experimental products. **8 a:** An overview of the intra-carbonate glass with Ca-rich glass forming a fine network of fracture in-fill and locally collecting in pools. Dendritic calcite crystals within the Ca-rich glass are also visible. **8 b:** At higher magnification, intra-carbonate glass can be seen to collect into pools and the nature of the termination points of the intra-carbonate veinlets is visible. **8 c:** Three generations of vesicles extending from the carbonate grain are shown, labelled Gen.1, 2, and 3. **8 d:** Ca-normal glass (dark grey) displays a ‘swirly’, mingled texture within the Ca-enriched glass (bright grey).

**Figure 9:** Comparison of an experiment run at P = 1 GPa (**9 a**) with a similar experiment run at 0.5 GPa (**9 b, also shown in Fig 3 j**). Both experiments were run with T = 1200°C, t<sub>d</sub> = 300s, using hydrous starting material and display the same major textural features. The carbonate has assimilated and given rise to two compositionally distinct domains of glass (the boundary between the 2 domains of glass is highlighted with white dashed lines for clarity). The sizes of the vesicles in these experiments constitute the maximum for all experiments reported in this study, and are confined to the Ca-enriched glass zones. Note that although the vesicles are larger in the 1GPa experiment, they are also fewer, which indicates a greater degree of coalescence in this experiment.

**Figure 10:** Selected BSE images displaying textural features within a representative set of natural Merapi calc-silicate xenoliths. Abbreviations: Pyx = pyroxene, Wo = wollastonite, Spu = spurrite.

**10 a:** Sample MXCS-0-c contains larnite with a pervasive micro-vesicular texture that grades into a slightly less calcic glassy zone towards wollastonite. **10 b:** Sample MXCS-0-g contains preserved carbonate bordered by glass with the composition of spurrite, which, in turn, is bordered by larnite.

**10 c:** Sample MXCS-0-g contains carbonate inclusions hosted in wollastonite. Similar to (a), a Ca-

gradation exists between the larnite and wollastonite. Numbers in (a), (b), and (c) are CaO wt% and volatiles present. See **Table 5** for representative analyses of minerals and glass in the xenoliths.

**Figure 11:** Ternary plot ( $\text{SiO}_2\text{-CaO-Al}_2\text{O}_3$ ) displaying glass analyses representative of all experiments in this study. Analyses of a representative natural Merapi calc-silicate xenolith are shown for comparison. Experimental data (1200°C, 0.5 GPa, anhydrous and hydrous, grey field on the plot): 374-4 (n = 23), 374-5 (n = 4), 375-6 (n = 11), 375-7 (n = 5), 376-10 (n = 32), 376-11 (n = 35), 379-16 (n = 11), 379-17 (n = 32), 386-18 (n = 45), 386-19 (n = 81), 387-20 (n = 41), 387-21 (n = 61). Merapi xenolith data (field with cross pattern on the plot): MXCS-a (n = 4), MXCS-b (n = 2), MXCS-c (n = 2), MXCS-g (n = 3). Note that the experimental melts range from relatively unaffected, Ca-normal composition (similar to the starting M-94 basaltic-andesite) to strongly contaminated, Ca-enriched glass.

Table 1: Composition of starting materials used in experiments

Sample	Average composition (EMP) of anhydrous M-94-a-107 glass <sup>1</sup>	Average composition (EMP) of hydrous M-94-a-107 glass <sup>2</sup>		Whole rock analysis (XRF) of limestone added <sup>4</sup>	
		1 $\sigma$ (10) <sup>3</sup>		1 $\sigma$ (9) <sup>3</sup>	
<i>wt%</i>					
SiO <sub>2</sub>	54.11	0.60	51.83	0.43	0.28
TiO <sub>2</sub>	0.85	0.09	0.89	0.05	0.01
Al <sub>2</sub> O <sub>3</sub>	18.98	0.17	18.08	0.24	0.13
FeO	7.89	0.56	8.17	0.16	0.01
MnO	0.24	0.03	0.20	0.03	0.00
MgO	2.98	0.13	2.97	0.08	0.40
CaO	8.89	0.17	9.19	0.16	56.72
Na <sub>2</sub> O	3.56	0.13	3.48	0.09	0.12
K <sub>2</sub> O	2.05	0.10	2.05	0.03	0.00
P <sub>2</sub> O <sub>5</sub>	0.29	0.04	0.34	0.04	0.03
Total	99.85		97.20		57.70
H <sub>2</sub> O	-		2.23		0.15
CO <sub>2</sub>	-		-		44.93

<sup>1</sup> Glass synthesised using M-94 whole rock powder in a Pt capsule at 1300°C, 1atm in air.

<sup>2</sup> M-94-a-107 glass uniformly hydrated at Universität Hannover (Germany) and measured for water content by Karl Fischer Titration (KFT).

<sup>3</sup> 1 $\sigma$  standard deviation; the number in parentheses represents the number of analyses for each sample.

<sup>4</sup> XRF analysis carried out at IFM-GEOMAR (Kiel, Germany).

Table 2: Experimental conditions and phases present in experiment

Run-Sample	P (GPa)	T (°C)	t <sub>d</sub> <sup>1</sup> (s)	M-94-a-107(mg)	CaCO <sub>3</sub> added (mg)	Phases present
379-16	0.5	1200	0	40.5	9.9	S (cc + x), M, V
379-17 <sup>2</sup>	0.5	1200	0	40.4	9.9	S (cc + crys), M, V
387-20	0.5	1200	60	38.3	9.6	S (cc + x), M, V
387-21 <sup>2</sup>	0.5	1200	60	41.7	10.0	S (cc + crys), M, V
376-10	0.5	1200	90	40.9	9.6	S (cc + x), M, V
376-11 <sup>2</sup>	0.5	1200	90	42.9	9.1	M, V
375-6	0.5	1200	150	42.5	10.1	S (cc + x), M, V
375-7 <sup>2</sup>	0.5	1200	150	42.7	10.3	M, V
374-4	0.5	1200	300	40.5	8.5	S (x), M, V
374-5 <sup>2</sup>	0.5	1200	300	42.6	9.3	M, V
386-18	0.5	1200	300	41.2	9.9	S (x), M, V
386-19 <sup>2</sup>	0.5	1200	300	41.3	9.9	M, V
374-8 <sup>3</sup>	0.5	1200	300	40.8	0.0	S (x), M, V (μ)
378-15 <sup>2,3</sup>	0.5	1200	300	30.0	0.0	M, V (μ)

<sup>1</sup> 't<sub>d</sub>' is an abbreviation for the dwell time of an experiment (i.e. the length of time that the experiment is held at 1200°C).

<sup>2</sup> Experiments carried out using the hydrated M-94-a-107 glass.

<sup>3</sup> Control experiments carried out with no added limestone.

Abbreviations used: t<sub>d</sub> (experiment dwell time); S (solid); cc (calcium carbonate); x (plagioclase crystals); crys (calcite crystallites); M (melt); V (volatiles, CO<sub>2</sub> and/or H<sub>2</sub>O); μ (micro bubbles only)

Table 3: Representative EMP analyses of experimentally-derived glasses

Run-Sample	Ca-normal glass				Ca-rich glass			
	379-17	376-11	386-19	374-5	379-17	376-11	386-19	374-5
<i>wt%</i>								
SiO <sub>2</sub>	51.97	51.62	52.28	50.83	34.11	27.72	34.90	38.08
TiO <sub>2</sub>	0.74	0.81	0.77	0.89	0.45	0.49	0.56	0.58
Al <sub>2</sub> O <sub>3</sub>	17.94	18.21	18.50	18.70	12.27	10.32	12.23	13.93
FeO	6.89	6.42	6.30	6.23	5.35	4.85	5.38	5.48
MnO	0.17	0.10	0.10	0.20	0.11	0.18	0.13	0.14
MgO	2.89	2.82	2.66	2.73	2.41	2.18	2.30	2.26
CaO	9.13	8.88	9.75	8.83	31.16	34.34	31.08	27.39
SrO	0.09	0.10	0.08	0.10	0.03	0.08	0.08	0.07
Na <sub>2</sub> O	3.94	4.54	3.66	4.48	1.35	1.33	1.75	2.22
K <sub>2</sub> O	2.40	2.48	2.50	2.26	0.73	0.65	0.79	1.21
P <sub>2</sub> O <sub>5</sub>	0.32	0.28	0.30	0.27	0.22	0.16	0.24	0.22
Total <sup>1</sup>	96.48	96.26	96.90	95.52	88.19	82.30	89.44	91.56
Run-Sample	Hybrid glass <sup>2</sup>				Inter-carbonate glass			
	379-17	376-11	386-19	375-5	379-17	379-17	379-16	387-21
<i>wt%</i>								
SiO <sub>2</sub>	46.25	41.15	50.72	49.18	31.19	30.23	36.45	34.68
TiO <sub>2</sub>	0.62	0.66	0.64	0.67	0.52	0.44	0.53	0.47
Al <sub>2</sub> O <sub>3</sub>	16.07	14.93	17.73	17.49	10.19	10.40	13.22	13.22
FeO	6.23	5.28	5.05	4.98	4.07	3.81	5.60	4.91
MnO	0.13	0.07	0.13	0.16	0.12	0.07	0.16	0.18
MgO	2.46	2.27	1.96	2.05	2.10	2.15	2.33	2.02
CaO	19.42	24.00	15.64	15.60	35.41	36.52	32.13	32.41
SrO	0.05	0.07	0.04	0.11	0.09	0.01	0.08	0.03
Na <sub>2</sub> O	2.35	2.07	2.81	3.54	2.46	2.60	1.73	1.74
K <sub>2</sub> O	1.33	1.01	2.01	2.18	1.45	1.44	0.89	0.86
P <sub>2</sub> O <sub>5</sub>	0.26	0.20	0.32	0.24	0.25	0.22	0.22	0.21
Total <sup>1</sup>	95.17	91.71	97.05	96.20	87.85	87.89	93.33	90.70

<sup>1</sup> Analysis totals are low (sometimes < 90 wt%) due to a combination of dissolved volatiles (mainly CO<sub>2</sub>) and unavoidable micro-bubbles.

<sup>2</sup> Glass with composition intermediate between the Ca-normal and Ca-rich end-members. Analyses shown are from the glass interfacial regions.

*Table 4: Strontium concentrations and isotope ratios in micro-milled experimental glass*

Experiment, location	Sr ppm	$^{87}\text{Sr}/^{86}\text{Sr}$	2 SE
<i>379-17 (0s)</i>			
1 (M73-3)	494	0.705641	0.000020
2 (M73-2)	472	0.705788	0.000008
3 (M73-4)	466	0.706361	0.000056
4 (M73-5)	500	0.705886	0.000106
<i>386-19 (300s)</i>			
1 (M73-7)	509	0.705675	0.000056
2 (M73-8)	370	0.706117	0.000020
3 (M73-9)	390	0.706532	0.000082
4 (M73-10)	420	0.706068	0.000030
5 (M73-11)	375	0.705893	0.000020

Location numbers refer to sampled areas in the experiments, as shown in Fig. 5.

Table 80mm wide, to fit one column.



Table 5: Representative EMP analyses of minerals and glass in Merapi xenoliths

Phase	Larnite	Spurrite	Glass border at Wo			Calcite	
Sample	MXCS-c	MXCS-g	MXCS-c	MXCS-g	MXCS-g	MXCS-a	MXCS-g
<i>wt%</i>							
SiO <sub>2</sub>	34.12	26.36	32.23	31.56	31.62	0.08	0.14
TiO <sub>2</sub>	0.05	0.02	0.05	0.03	0.03	0.00	0.00
Al <sub>2</sub> O <sub>3</sub>	0.07	0.08	0.00	0.07	0.05	0.01	0.25
FeO	0.09	0.04	0.04	0.00	0.07	0.02	0.05
MnO	0.00	0.00	0.01	0.00	0.06	0.01	0.19
MgO	0.01	0.00	0.02	0.00	0.01	0.01	0.04
CaO	65.97	62.71	61.57	61.44	62.08	56.81	47.55
Na <sub>2</sub> O	0.00	0.03	0.03	0.00	0.01	0.00	0.04
K <sub>2</sub> O	0.00	0.01	0.00	0.01	0.02	0.00	0.01
P <sub>2</sub> O <sub>5</sub>	0.04	0.05	0.02	0.06	0.03	0.04	0.02
Total <sup>1</sup>	100.35	89.30	93.97	93.17	93.98	56.98	48.29
Phase	Wollastonite	Pyroxene	Plag An <sub>98</sub>	Sphene	High-Si interstitial glass		
Sample	MXCS-b	MXCS-1A	MXCS-b	MXCS-b	MXCS-1A	MXCS-1A	MXCS-1B
<i>wt%</i>							
SiO <sub>2</sub>	50.83	51.88	43.34	32.24	72.44	73.49	75.29
TiO <sub>2</sub>	0.00	0.03	0.12	38.25	0.36	0.24	0.18
Al <sub>2</sub> O <sub>3</sub>	0.24	0.44	35.52	1.41	12.80	12.54	11.81
FeO	0.63	14.85	0.29	0.73	2.36	2.06	1.92
MnO	0.40	0.40	0.01	0.11	0.04	0.04	0.06
MgO	0.14	8.51	0.00	0.00	0.06	0.05	0.02
CaO	47.71	23.86	20.21	27.58	3.23	3.57	2.49
Na <sub>2</sub> O	0.02	0.07	0.18	0.00	3.45	3.20	3.07
K <sub>2</sub> O	0.00	0.01	0.01	0.00	4.13	3.75	4.20
P <sub>2</sub> O <sub>5</sub>	0.05	0.03	0.06	0.22	0.00	0.04	0.00
Total	100.02	100.08	99.74	100.54	98.87	98.98	99.04

<sup>1</sup> Analysis totals for the glassy border zones in the xenoliths are low (< 95wt%) due to dissolved volatiles. Calcite and spurrite totals are low due to their CO<sub>2</sub> component.

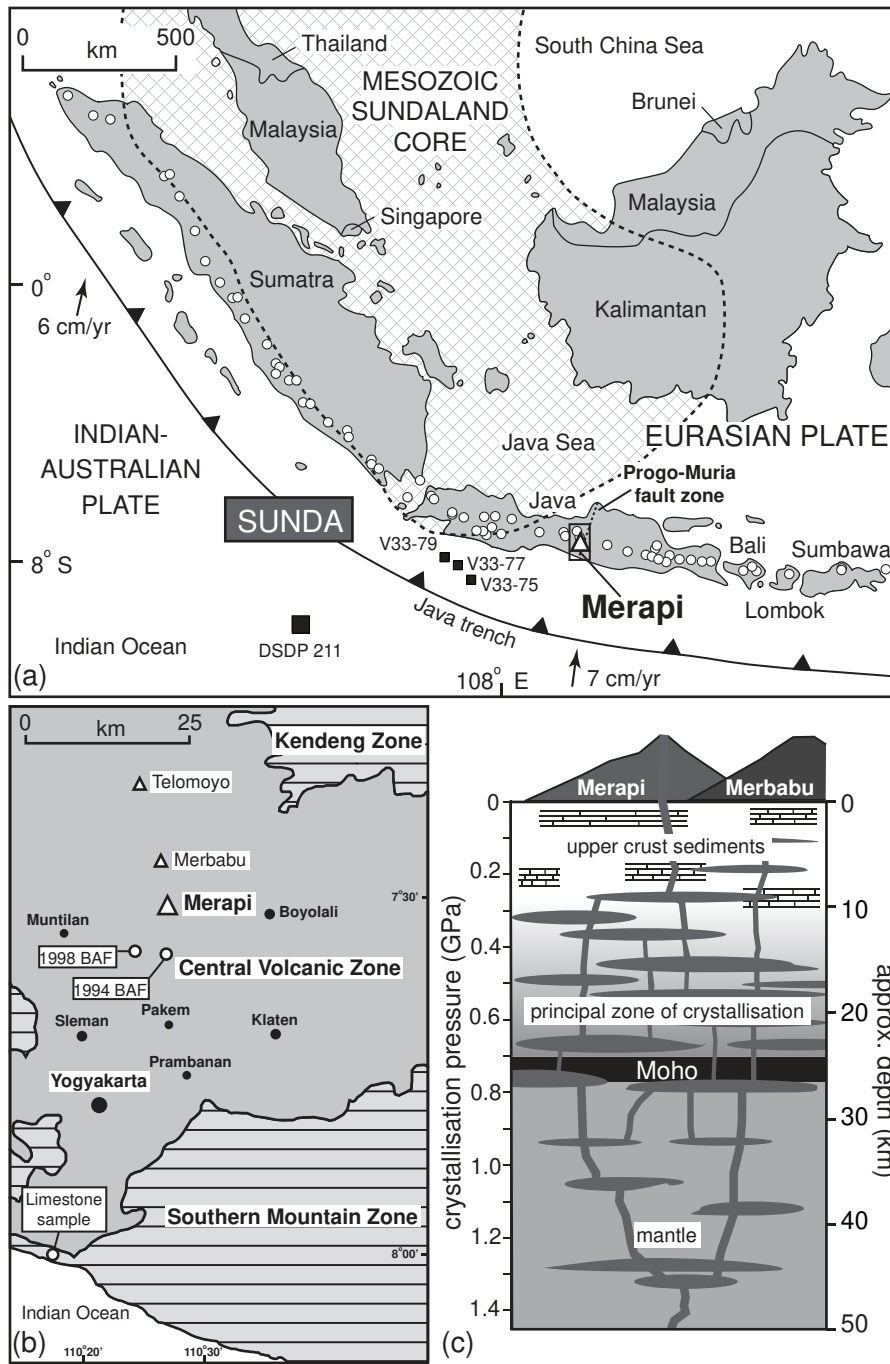


Fig 1

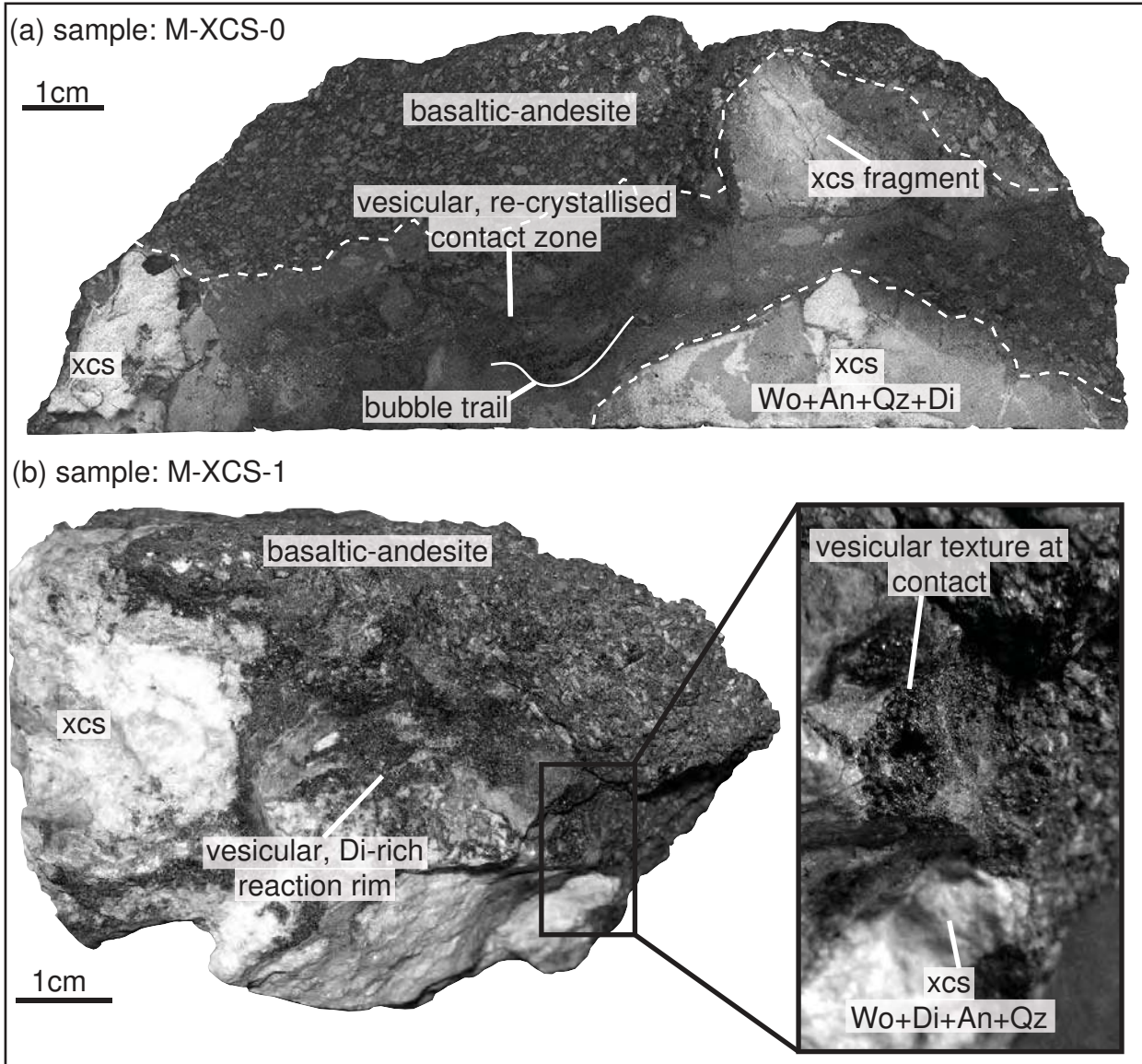


Fig 2

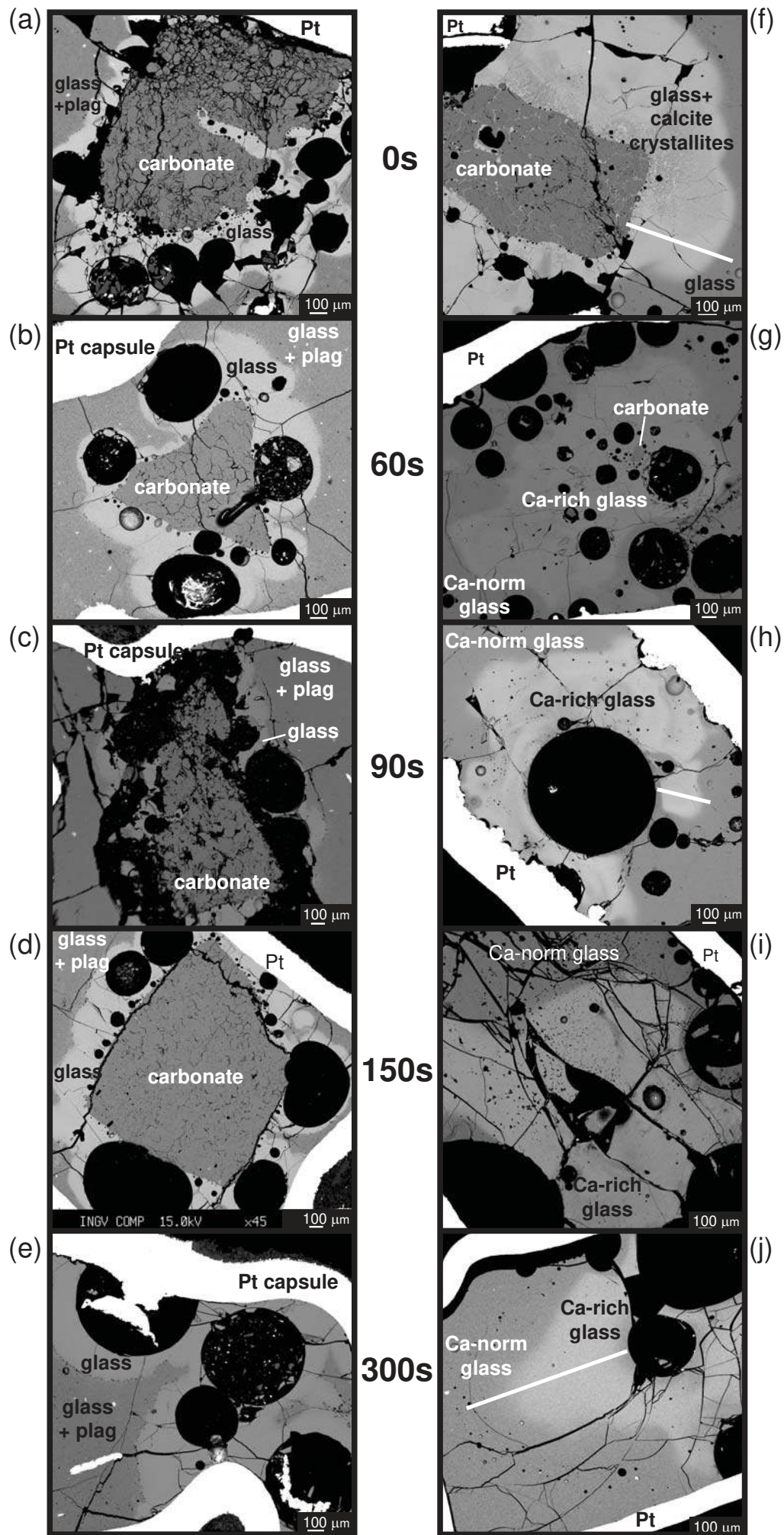


Fig 3



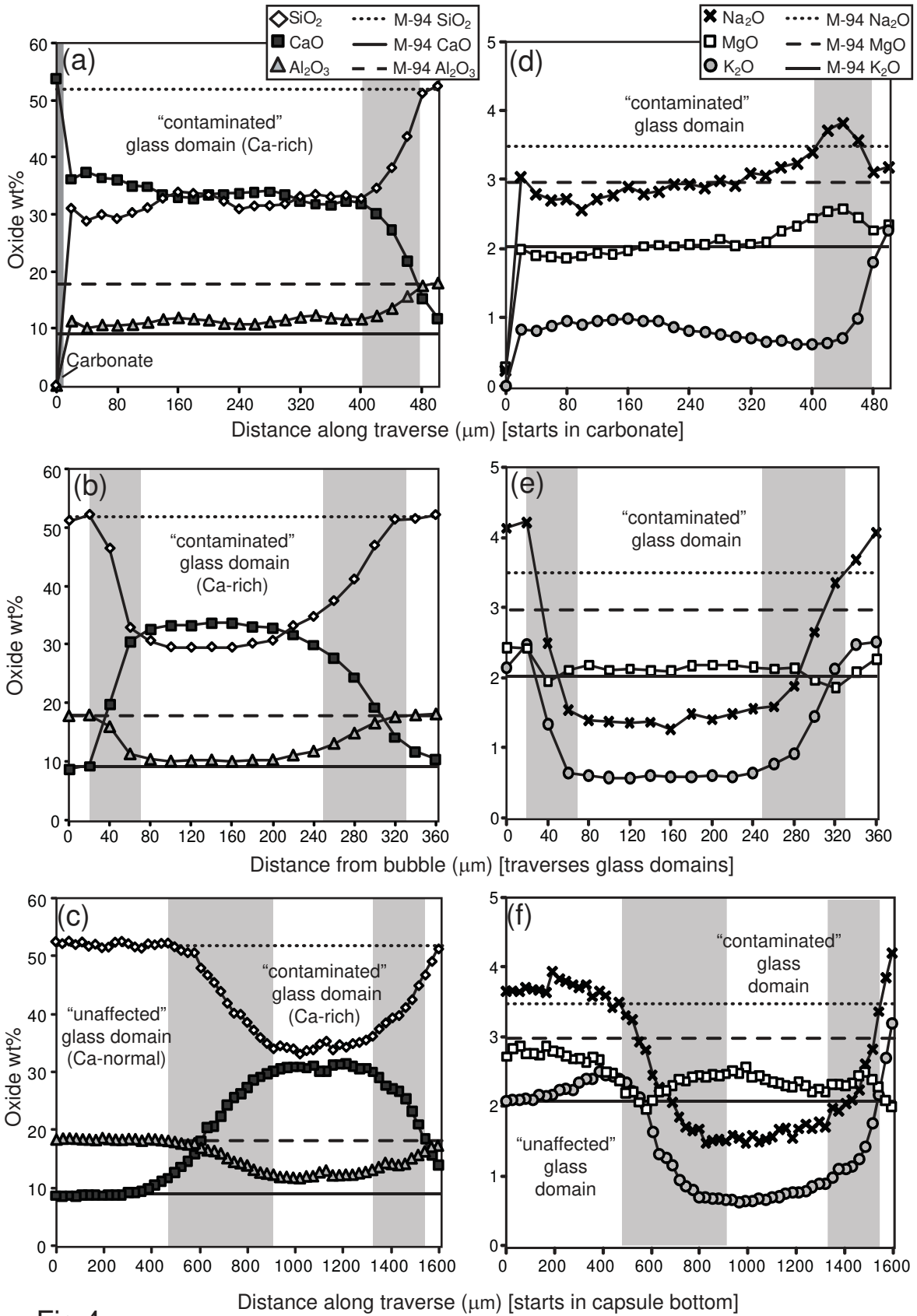


Fig 4

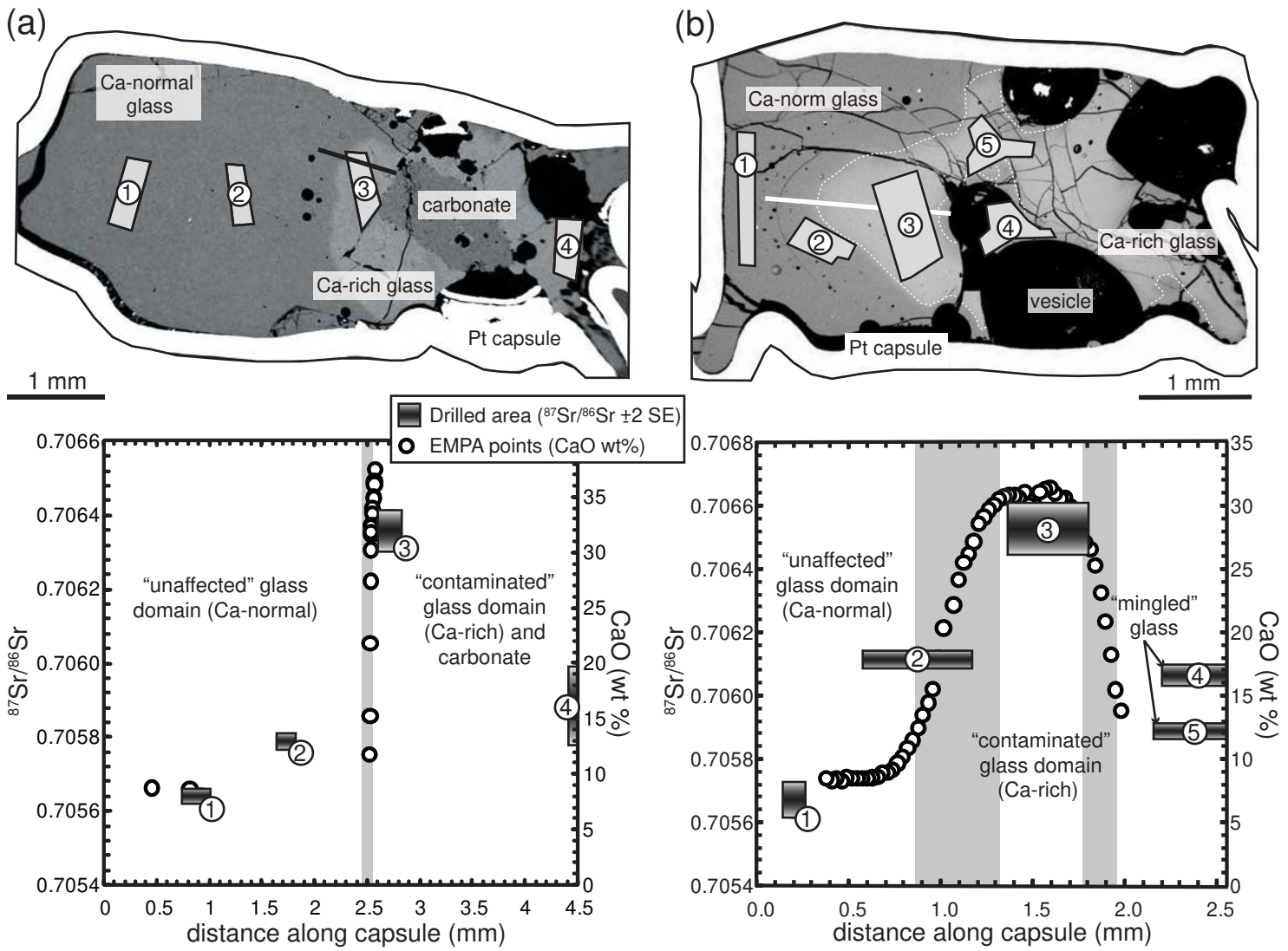


Figure 5

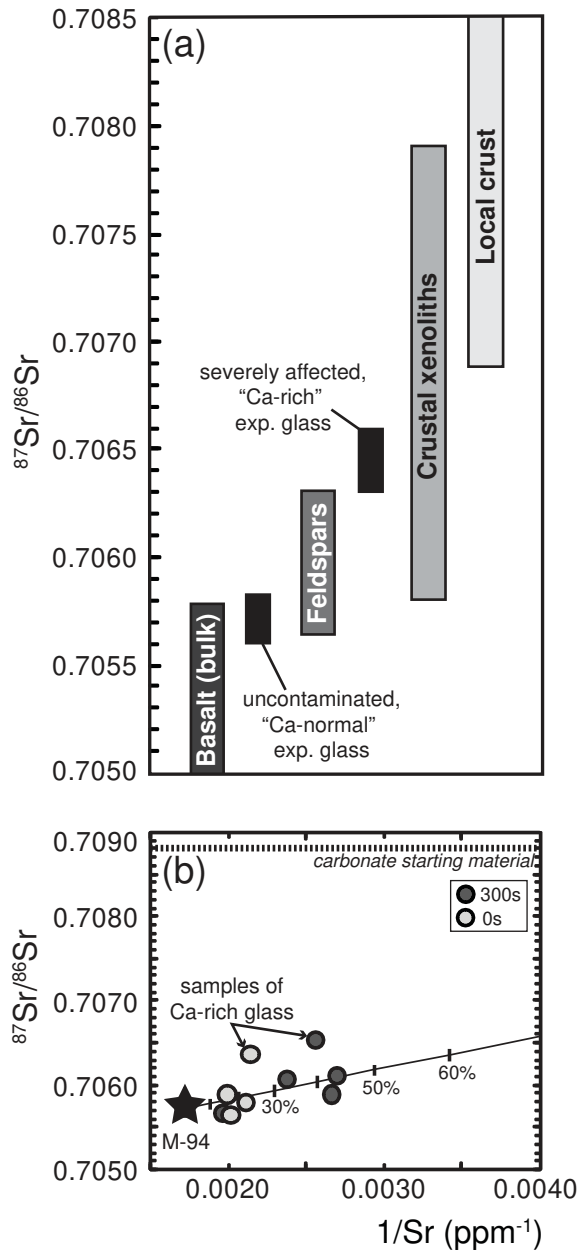


Fig 6

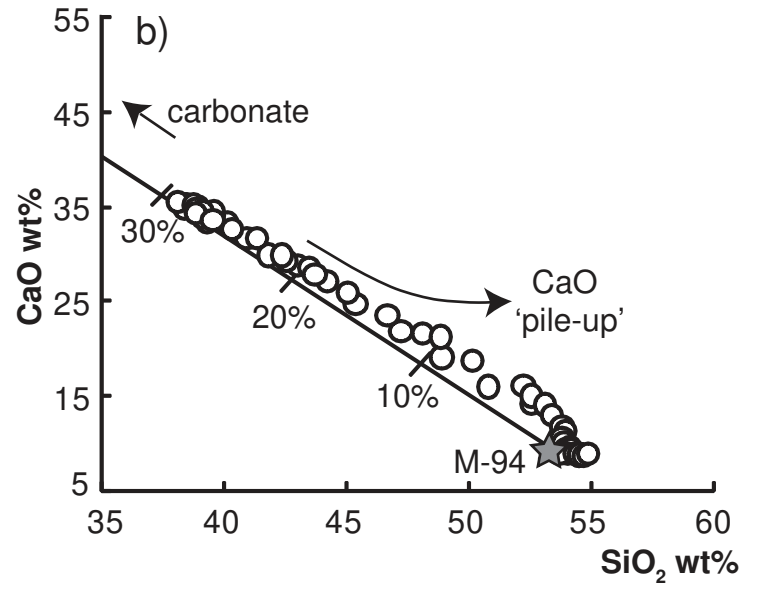
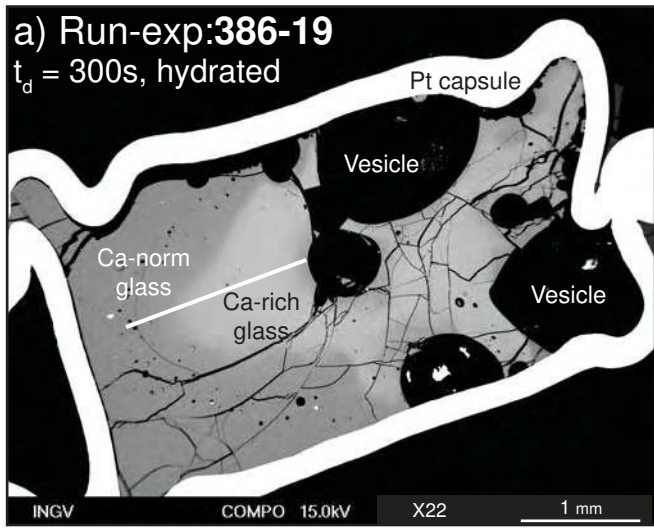
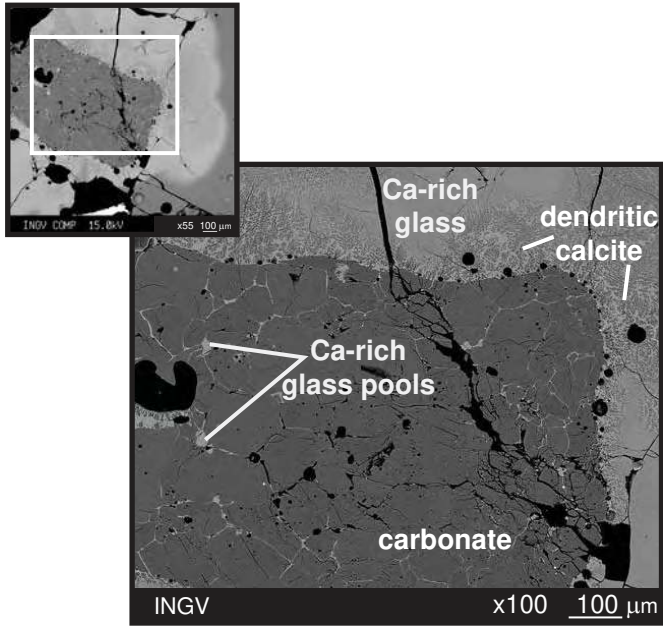


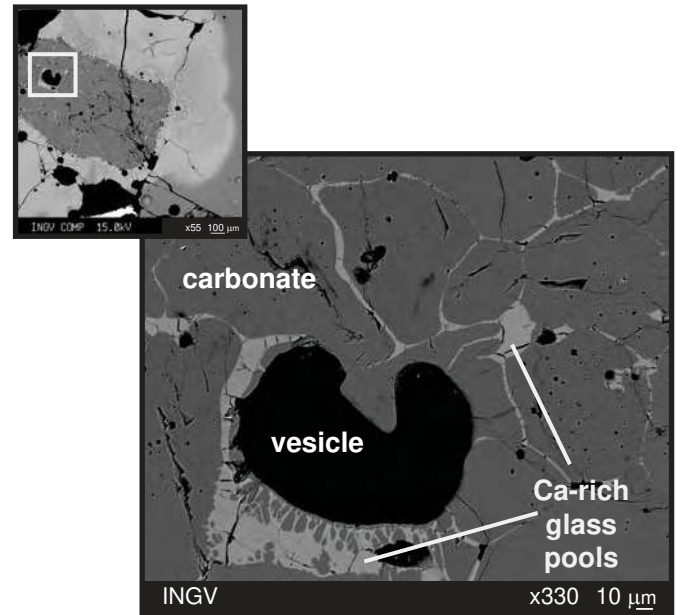
Fig 7



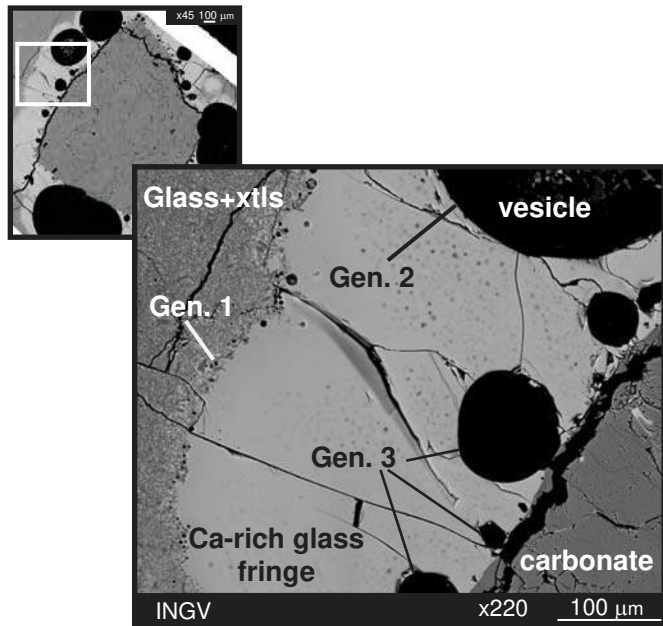
(a)  $t_d = 0s$ , hydrous



(b)  $t_d = 0s$ , hydrous



(c)  $t_d = 150s$ , anhydrous



(d)  $t_d = 0s$ , anhydrous

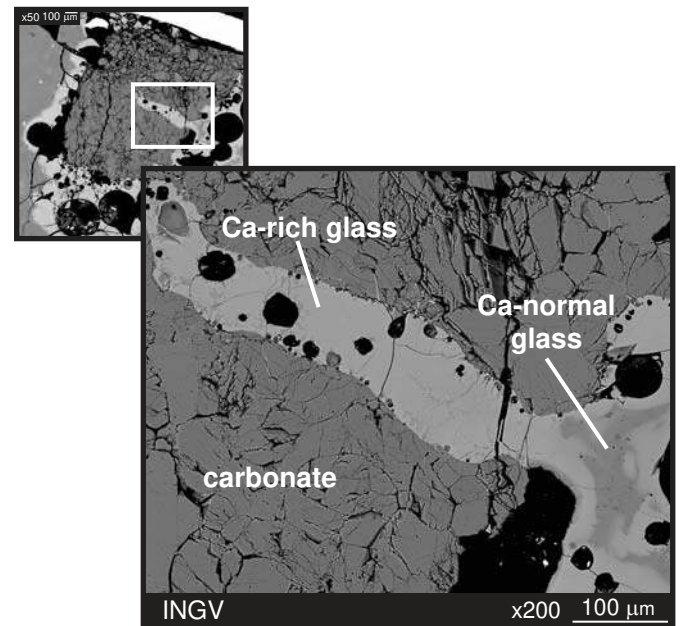


Fig 8

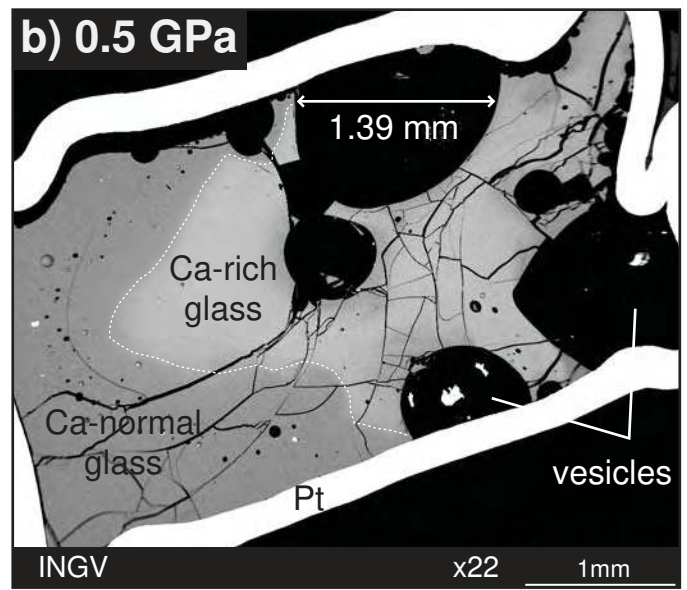
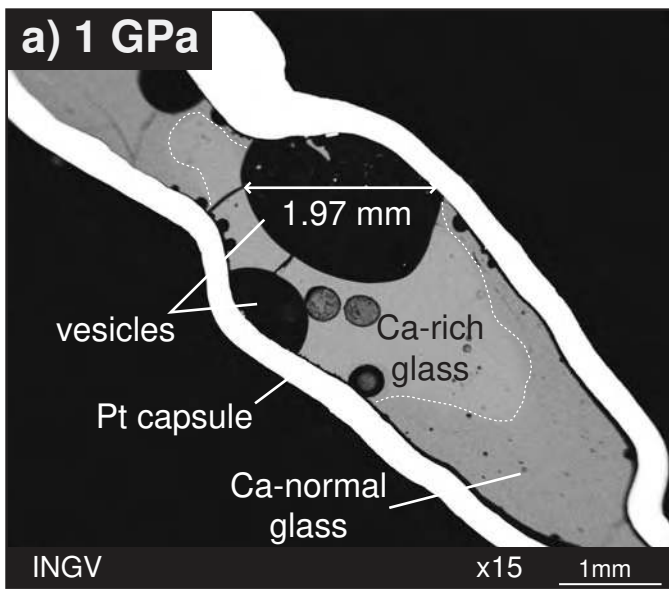


Fig 9

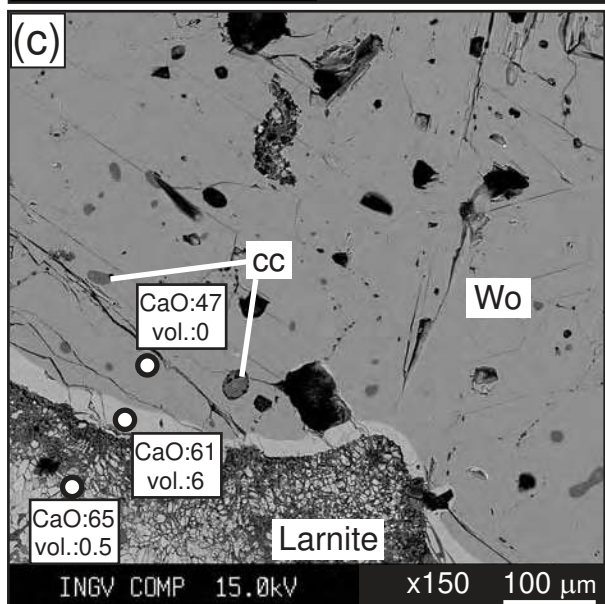
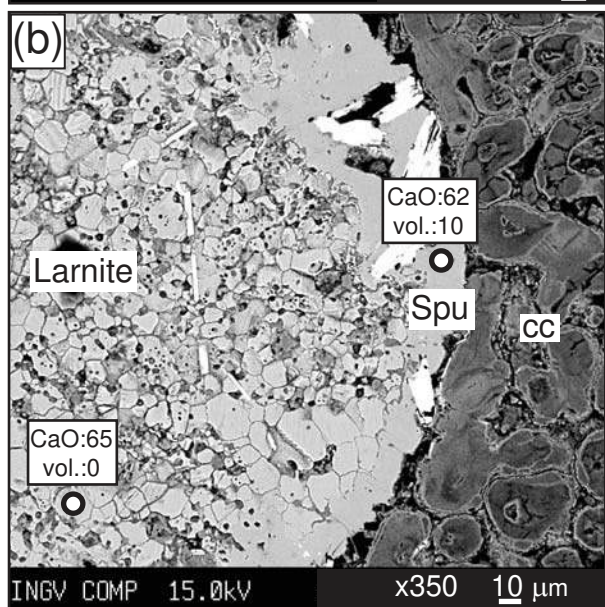
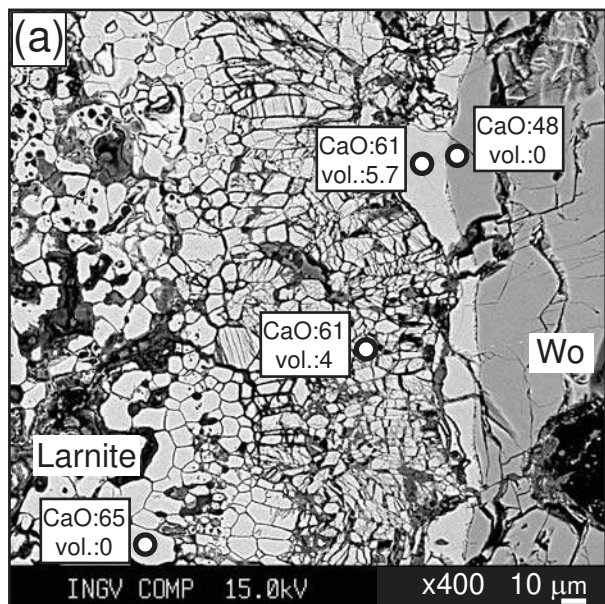


Fig 10

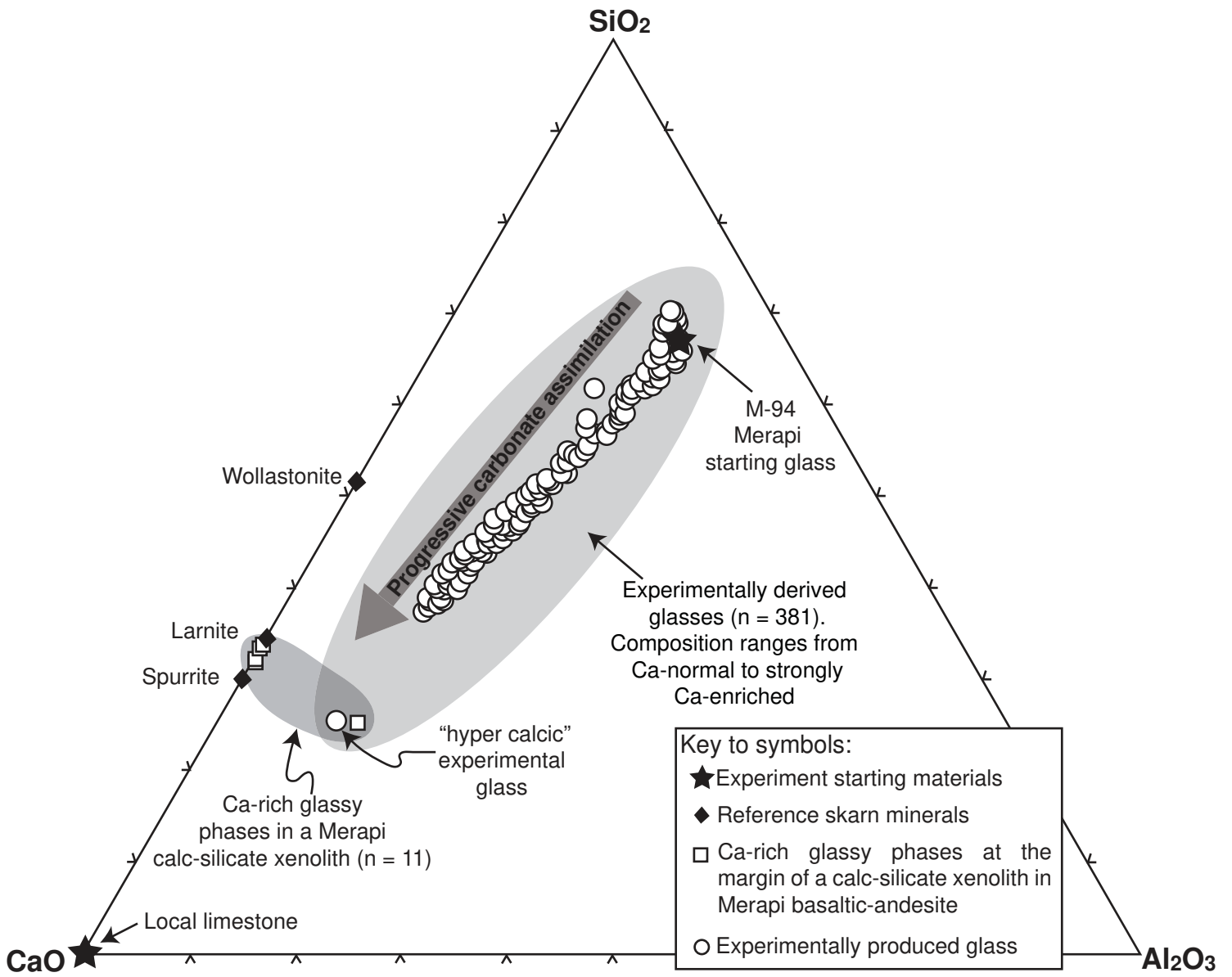


Fig 11